J. Fluid Mech. (2023), *vol*. 956, A2, doi:10.1017/jfm.2022.996

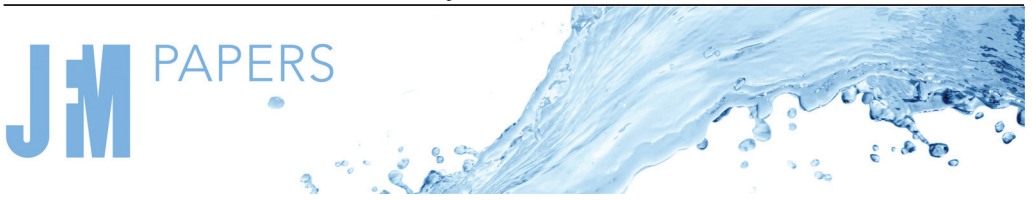

Acoustic resonance mechanism for axisymmetric screech modes of underexpanded jets impinging on an inclined plate

Xiangru Li[1,2], Xuecheng Wu[1,2], Luhan Liu[1,2], Xiwen Zhang[1,2], Pengfei Hao[1,2] and Feng He[1,2,†]

[1]Department of Engineering Mechanics, School of Aerospace Engineering, Tsinghua University, Beijing 100084, PR China

[2]Applied Mechanics Laboratory, Department of Engineering Mechanics, Tsinghua University, Beijing 100084, PR China

(Received 13 June 2022; revised 25 September 2022; accepted 18 November 2022)

In this paper, the acoustic resonance mechanism for different axisymmetric screech modes of the underexpanded jets that impinge on an inclined plate is investigated experimentally. The ideally expanded Mach number of jets (M_j) ranges from 1.05 to 1.56. The nozzle-to-plate distance at the jet axis and the impingement angle are respectively set as 5.0D and 30°, where D is the nozzle exit diameter. The acoustic results show that the M_j range for the A2 screech mode of impinging jets is broader than that of underexpanded free jets, and a new axisymmetric screech mode A3 appears. With the increase of M_j, the effect of the impinging plate on the shock cell structures of jets becomes obvious gradually, and the second suboptimal peaks are evident in the axial wavenumber spectra of mean shock structures. The coherent flow structures at screech frequencies are extracted from time-resolved schlieren images via the spectral proper orthogonal decomposition (SPOD). The axial wavenumber spectra of the selected SPOD modes suggest that the A1, A2 and A3 screech modes are respectively closed by the guided jet modes that are energized by the interactions between the Kelvin–Helmholtz wavepacket and the first three shock wavenumber peaks. The upstream- and downstream-propagating waves that constitute the screech feedback loop are analysed by applying wavenumber filters to the wavenumber spectra of SPOD modes. The frequencies of these three screech modes can be predicted by the phase constraints between the nozzle exit and the rear edge of the third shock cell. For the A3 mode, the inclined plate invades the third shock cell with the increase of M_j, and the phase constraint cannot be satisfied at the lower side of the jets, which leads the A3 mode to fade away. The present results suggest that external boundaries can modulate the frequency and mode of jet screech by changing the axial spacings of shock cells.

Key words: jet noise, high-speed flow, jets

† Email address for correspondence: hefeng@tsinghua.edu.cn

1. Introduction

Shock-containing supersonic jets often generate high-intensity tones at discrete frequencies, such as the screech tones of underexpanded free jets (Tam 1995; Raman 1999) and impingement tones generated by the jets that impinge on a plate (Henderson & Powell 1993; Edgington-Mitchell 2019). It is widely recognized that the discrete tones generated in underexpanded jets are due to the acoustic feedback loops that are established in the flow (Edgington-Mitchell 2019). The self-sustaining feedback loop in underexpanded jets can be divided into four physical processes (Raman 1999; Edgington-Mitchell 2019): the downstream propagation of instability waves, the generation process of upstream-propagating disturbances, the upstream propagation of disturbances, and the receptivity process near the nozzle exit. The downstream-propagating component of the feedback loop is generally thought to be the Kelvin–Helmholtz (K–H) wavepacket (Jordan & Colonius 2013), which extracts energy from the mean flow to maintain the feedback loop (Tam & Ahuja 1990). Using the adjoint equation approach, Barone & Lele (2005) developed a framework for the receptivity analysis of compressible free shear flows. Mitchell, Honnery & Soria (2012) investigated experimentally the receptivity process near the nozzle exit for supersonic impinging jets. The schlieren images recorded by ultra-high-speed cameras showed that the arrival of upstream-propagating acoustic waves at the nozzle lip generates sinusoidal disturbances in the jet shear layer, then these disturbances grow into the downstream-propagating coherent structures. Karami *et al.* (2020) investigated the receptivity near the nozzle exit of underexpanded impinging jets by solving the linearized three-dimensional Navier–Stokes equations. The azimuthal mode numbers and Strouhal numbers of the external disturbances that have the highest receptivity are determined by a transfer function defined as the ratio of the output flow energy to the input energy of the acoustic disturbance.

1.1. *Sound-generation and resonance-closure mechanisms for underexpanded free jets*

The screech frequencies of underexpanded free jets decrease steadily with the increase of the nozzle pressure ratio (NPR). But at some particular NPR ranges, abrupt jumps of screech frequencies appear (Powell 1953). For screeching axisymmetric jets, as the degree of jet underexpansion is increased, the instability mode of jets changes successively from the axisymmetric A1 mode to another axisymmetric A2 mode, a flapping B mode, a helical C mode, and finally another flapping D mode (Powell 1953; Davies 1962; Powell, Umeda & Ishii 1992; Li *et al.* 2020).

Powell (1953) first described the screech phenomenon of axisymmetric underexpanded free jets, and proposed that the screech tone was generated from a series of monopole sources that are located at the shock tips. The phase relationship between these sources leads to the directive radiation of screech tone in the upstream direction. The weakest link model of Tam & Tanna (1982) suggested that the interaction between the K–H wavepacket and the shock cells produces two wave-like disturbances whose wavenumbers are respectively the sum and difference of the wavenumbers of the K–H wavepacket (k_h) and the shock cells (k_s). The phase velocity of the disturbances can be negative and supersonic when k_h and k_s are close (Tam, Parrish & Viswanathan 2014). The supersonic disturbances lead to the production of upstream-propagating acoustic waves via the Mach wave radiation (Tam 2009). The shock-leakage theory (Manning & Lele 1998; Suzuki & Lele 2003; Shariff & Manning 2013) explains the physical mechanism of how the interaction between a vortex in the shear layer and a shock generates acoustic waves. For underexpanded free jets, the shock-leakage phenomenon has been observed in the

large eddy simulation of a planar jet (Berland, Bogey & Bailly 2007) and in the schlieren visualizations of round jets (Edgington-Mitchell *et al.* 2021*b*).

The upstream-propagating component in the screech feedback loop of underexpanded free jets is traditionally considered as the upstream-propagating freestream acoustic waves. Shen & Tam (2002) first proposed that the upstream-propagating guided jet modes (Tam & Hu 1989) could act as the upstream-travelling waves in the feedback loops for the A2 and C screech modes. In recent years, Edgington-Mitchell *et al.* (2018) and Gojon, Bogey & Mihaescu (2018) provided experimental and numerical evidence to support that the screech feedback loops in the A1, A2 and C modes are closed by the guided jets modes. For the A1 and A2 screech modes, the screech frequency prediction models based on the guided jet mode (Mancinelli *et al.* 2019, 2021) provide a better agreement with experimental observations than other models in which the feedback loop is closed by the freestream acoustic waves. Edgington-Mitchell *et al.* (2021*a*) investigated the interaction between various wave-like structures in screeching jets via experimental measurements and linear stability analyses. They demonstrated that the upstream-propagating guided jet modes are energized by the interaction between the K–H wavepacket and shock cells in screeching jets. Recently, Nogueira *et al.* (2022*b*) conducted linear stability analyses on shock-containing jets by taking a spatially periodic mean flow as a surrogate of shock cells. An absolute instability mechanism between the K–H mode and the upstream-propagating guided jet mode is discovered. The frequencies and mode shapes related to the absolute instability have good agreement with the screech frequencies and the most energetic coherent structures of screeching jets. Then, via a similar methodology, Nogueira *et al.* (2022*a*) also suggested that the A1 screech mode is closed by the guided jet mode generated by the interaction between the K–H mode and the primary wavenumber of the averaged shock structures. The A2 mode is associated with the interaction between the K–H wavepacket and the first suboptimal wavenumber peak of the shock structures. Furthermore, Edgington-Mitchell *et al.* (2022) demonstrated that the upstream-propagating guided jet modes are shown to be active in all stages of screech, and the mode staging of screech tone can be due to either a change in which peak of the shock spectra the K–H wavepacket is interacting with, or a change in azimuthal mode, or both.

1.2. *Acoustic resonance of vertical jet impingement*

Because of the existence of the plate, the flow structures of underexpanded impinging jets are more complex (Henderson 2002). The staging behaviour of impinging tones is dependent largely on the NPR and the nozzle-to-plate spacing (Edgington-Mitchell 2019). Multiple intense tones are often present simultaneously in impinging jets (Henderson & Powell 1993), and sometimes, the impinging tones that are produced for the plate spacings between $5D$ and $10D$ are related to the jet screech (Henderson 2002).

Several theories are proposed to explain the generation process of upstream-propagating disturbances in underexpanded impinging jets. Henderson (2002) suggested that the oscillation of the standoff shock is responsible for the production of upstream-propagating waves in both small- and large-plate impingement. Nevertheless, discrete tones are also observed in subsonic impinging jets (Tam & Ahuja 1990). This means that the interaction between the downstream-propagating K–H wavepacket and the impinging plate can produce intense tones in the absence of shock structures. Henderson, Bridges & Wernet (2005) examined the generation process of impinging tones via phase-locked particle image velocimetry measurements. They demonstrated that the tones are generated in the wall jet at radial distance $1.3D$. The oscillations of the boundary of the wall jet lead to the production of upstream-propagating waves. Weightman *et al.* (2017*b*) proposed that the

periodic transient shocks in the wall jet of underexpanded impinging flows are responsible for the production of the impinging tone. The time delay between the inception of the shock and the formation of the acoustic wave also explains the phase lag in the phase criterion of feedback loop. However, Bogey & Gojon (2017) conducted numerical simulations on supersonic impinging round jets, and they observed that upstream-propagating acoustic waves are produced in the region of jet impingement. Additionally, in the experiments of Weightman *et al.* (2017*a*), acoustic waves are observed to be produced at the edges of the standoff shock, which is like the shock-leakage phenomena.

Tam & Ahuja (1990) first evidenced the role of the upstream-propagating guided jet modes in the resonance loop of subsonic impinging jets. In the numerical studies of Gojon, Bogey & Marsden (2016) and Bogey & Gojon (2017), by combining the feedback model (Ho & Nosseir 1981) and the dispersion relations of upstream-propagating guided jet modes, the tone frequencies, the mode number of the feedback loop, and the oscillation modes of ideally expanded supersonic impinging jets are well determined. However, in the experimental investigations of Henderson *et al.* (2005) and Weightman *et al.* (2017*b*), visualizations of flow fields showed that freestream acoustic waves travel to the nozzle exit outside the jet, perturb the shear layer and close the feedback loop.

1.3. *Jet impingement on an inclined plate*

There are numerous instances of supersonic jet impingement against an angled surface (Edgington-Mitchell 2019). When supersonic jets impinge on inclined flat plates, the flow structures are shown to be highly complex due to the local structure of the free jet and the interactions between shock waves in the free jet and those created by the plate (Lamont & Hunt 1980). The flow and acoustic fields of ideally expanded supersonic jets impinging on an inclined flat plate were investigated extensively. At least three types of acoustic waves are observed in the flow fields: Mach waves generated from the shear layer of main jets, acoustic waves generated from the impingement region, and Mach waves generated from the shear layer of the supersonic flow downstream of the jet impingement (Nonomura, Goto & Fujii 2011). The source locations and possible mechanism of the second type of acoustic waves are investigated further in Nonomura *et al.* (2016). Akamine *et al.* (2015) studied the propagation directions, the spectra, and the extent of the source regions of the acoustic waves using the results of microphone measurements and schlieren visualizations. Brehm, Housman & Kiris (2016) proposed that the noise generation in the jet-impingement region is attributed to vortex stretching and tearing, and shock oscillations induced by the motion of downstream-propagating coherent structures, and the noise generation in the wall jet is associated with supersonically convecting large-scale coherent flow structures. Several tones are produced when planar supersonic jets impinge on inclined plates, and these tones are due to the feedback mechanism between the nozzle lips and the flat plate (Gojon & Bogey 2019). Based on amplitude fields and velocity spectra in the jet shear layer, the feedback mechanism seems to be established mainly along the lip farther away from the plate. However, the acoustic resonance mechanism of the underexpanded jets that impinge on an inclined plate is not been investigated extensively.

The K–H wavepacket and shock cell structures also exist in the flow fields of underexpanded impinging jets. The interaction between the K–H wavepacket and shock cell structures, and the absolute instability mechanism between the K–H mode and the upstream-propagating guided jet mode, might also be associated with the acoustic resonance in impinging jets. It is natural that the spatial characteristics of shock structures are altered by the appearance of the impinging plate, and so are the frequencies and instability modes of acoustic resonances. In the present paper, the resonance mechanism

and mode staging process for the axisymmetric screech modes of underexpanded jets that impinge on an inclined plate are studied experimentally. The paper is organized as follows. An introduction to the experimental set-up and the post-processing methods of experimental results are given in § 2. In § 3, experimental results of acoustic measurements and schlieren visualizations are displayed in detail. The influence of the impinging plate on the averaged shock structures is analysed. The flow structures that are associated with the generation of tones are extracted, and a discussion on the mode staging mechanism is presented. The screech frequencies of different modes are predicted by the phase criterion of the acoustic feedback loop. Concluding remarks are given in § 4.

2. Experimental set-up and post-processing methods

2.1. *Experimental set-up*

The experimental facilities and instruments used in the present study are shown schematically in figure 1. These facilities are optimized for schlieren visualizations and not anechoic. The cases considered here are cold jets issuing from a converging nozzle that has exit diameter $D = 10$ mm and contraction ratio 6.25 : 1. The external lip thickness of the nozzle is 5 mm ($0.5D$). This nozzle lip thickness is intermediate compared with those used in the experiments of Powell *et al.* (1992) and Weightman *et al.* (2019). The inner wall of the nozzle is smooth, and the jets are not tripped. As presented in figure 1(*b*), underexpanded jets impinge on an inclined plate with an impingement angle of 30° in the present experiments. This impinging plate is a round aluminium plate with diameter $50.0D$. At the jet centreline, the impinging distance is set as $5.0D$, and the impinging distances at the upper and lower lip lines are $5.9D$ and $4.1D$, respectively. The static pressure $5D$ upstream of the nozzle exit is measured by using a COSMO digital pressure gauge. The measurement range of this pressure gauge is from 0 to 1.000 MPa, and the accuracy is 0.25 % of full scale. The total pressure upstream of the nozzle (p_0) is further calculated based on isentropic flow relations. The NPR is defined as the ratio between p_0 and the ambient pressure p_∞, and ranges from 2.0 to 4.0. The corresponding range of the ideally expanded jet Mach number M_j is [1.05, 1.56]. The Reynolds number $Re_j = \rho_j U_j D/\mu_j$ ranges from 2.1×10^5 to 2.7×10^5, where ρ_j, U_j and μ_j are respectively the ideally expanded jet density, velocity and dynamic viscosity.

Acoustic measurements are conducted by using a 1/4 inch diameter condenser microphone (Ono Sokki MI-1531) and a preamplifier (Ono Sokki MI-3140) with frequency range 10 Hz–100 kHz. As shown in figure 1(*a*), the microphone is located at angle 120° (measured from the downstream axis) and distance $50D$ from the nozzle exit. The microphone is calibrated by a sound calibrator (Ono Sokki SC-3120) prior to the measurements. The acoustic signals are analysed by using a fast Fourier transform (FFT) analyser (Ono Sokki CF-9400). A Hanning window function with 50 % overlap is used. The FFT analysis provides the noise spectra with highest frequency 100 kHz. These noise spectra are averages of 20 samples. The frequency resolution of the noise spectra is 62.5 Hz.

The time-resolved schlieren images are obtained by using a Photron Fastcam SA-Z high-speed camera. The frame rate of the camera is set as 80 000 frames per second. For the vast majority of cases in the present study, at least four images are recorded during a single period of the dominant screech tone. At this frame rate, the schlieren images are recorded with array size 640×360 pixels. 48 pixels are contained in the range of the nozzle diameter. By considering the frame rate and the light intensity, the exposure time

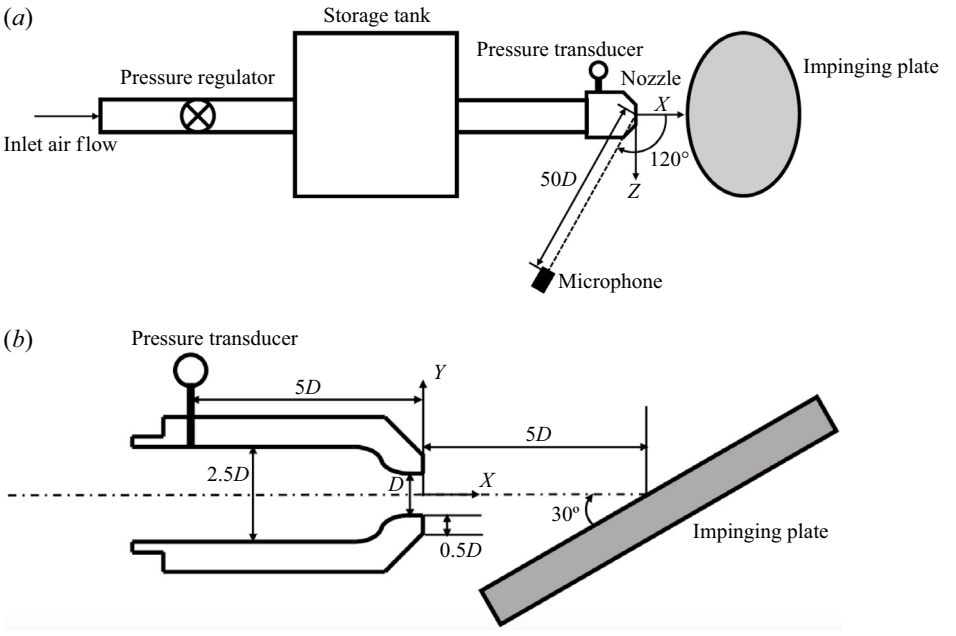

Figure 1. Schematics of (*a*) the test facilities and (*b*) the nozzle and impinging plate.

is set as 6.25 μs. The knife edge is set perpendicular to the jet axis. Variations of axial density gradients integrated along the optical path are observed in the current schlieren images.

2.2. *Decomposition of schlieren data*

The time-resolved schlieren image sequences contain a wealth of information about the flow dynamics (Edgington-Mitchell *et al.* 2021*b*). Spectral proper orthogonal decomposition (SPOD) introduced by Towne, Schmidt & Colonius (2018) is a model analysis method to extract coherent structures or modes from experimental and computational flow data. Each SPOD mode oscillates at a single frequency. SPOD combines the advantages of the dynamic mode decomposition (Schmid 2010) in terms of the temporal correlation among the resulting modes with the optimality and orthogonality of the standard proper orthogonal decomposition (Schmidt & Colonius 2020). Here, in order to educe the information of schlieren images associated with the acoustic resonance of impinging jets, SPOD is applied on the greyscales of schlieren sequences $\boldsymbol{G}$. The specific algorithm for computing SPOD modes from flow snapshots can be found in Towne *et al.* (2018) and Schmidt & Colonius (2020). For the sake of completeness, the algorithm is outlined here briefly. The vector $\boldsymbol{g}_i \in \mathbb{R}^N$ represents the instantaneous greyscales of a schlieren image at time t_i, which we call a snapshot of the flow. The length N of the vector is the number of pixels in a schlieren image. Now, M flow snapshots with an equal time spacing are recorded by the high-speed camera. This data set can be represented by the data matrix

$$\boldsymbol{G} = [\boldsymbol{g}_1, \boldsymbol{g}_2, \ldots, \boldsymbol{g}_M] \in \mathbb{R}^{N\times M}. \tag{2.1}$$

Subsequently, $\boldsymbol{G}$ is divided into a set of smaller and overlapping blocks as follows:

$$\boldsymbol{G}^{(n)} = [\boldsymbol{g}_1^{(n)}, \boldsymbol{g}_2^{(n)}, \ldots, \boldsymbol{g}_{N_f}^{(n)}] \in \mathbb{R}^{N\times N_f}, \tag{2.2}$$

where $\boldsymbol{G}^{(n)}$ is the nth block, consisting of N_f flow snapshots. The ith entry in $\boldsymbol{G}^{(n)}$ is $\boldsymbol{g}_{i+(n-1)(N_f-N_o)}$, where N_o is the number of snapshots by which the blocks overlap. The total number of blocks N_b can be calculated as $\lfloor (M-N_o)/(N_f-N_o) \rfloor$, where $\lfloor \cdot \rfloor$ denotes the floor operator. The discrete Fourier transform (DFT) is computed for each block in the temporal direction. To reduce spectral leakage, a Hanning window is used in the present analyses. Also, $\hat{\boldsymbol{g}}_j^{(n)}$ is the Fourier component at frequency f_j in the nth block. All realizations at a given frequency f_j are collected into the new data matrix

$$\hat{G}_{f_j} = [\hat{\boldsymbol{g}}_j^{(1)}, \hat{\boldsymbol{g}}_j^{(2)}, \ldots, \hat{\boldsymbol{g}}_j^{(N_b)}]. \tag{2.3}$$

SPOD eigenvectors and eigenvalues are obtained by solving the eigenvalue problem

$$\hat{G}_{f_j}^{*} \boldsymbol{W} \hat{G}_{f_j} \boldsymbol{\Theta}_{f_j} = \boldsymbol{\Theta}_{f_j} \boldsymbol{\Lambda}_{f_j}, \tag{2.4}$$

where $\boldsymbol{W}$ is the weight matrix. Then the SPOD modes for a given f_j can be obtained from the eigenvectors $\boldsymbol{\Theta}_{f_j}$ as $\hat{\boldsymbol{\Psi}}_{f_j} = \hat{G}_{f_j} \boldsymbol{\Theta}_{f_j} \boldsymbol{\Lambda}_{f_j}^{-1/2}$, and the diagonal matrix of eigenvalues $\boldsymbol{\Lambda}_{f_j}$ contains the energy of the SPOD modes.

Coherent structures at a specific frequency f_j are contained in the SPOD modes $\hat{\boldsymbol{\Psi}}_{f_j}$. These structures can be associated with a broad range of wavenumbers. The DFT in the jet axial direction is conducted on a chosen SPOD mode $\hat{\boldsymbol{\psi}}_{f_j}(x, y)$. Within the axial domain defined as $[x_1, x_2]$, the spatial Fourier coefficients $\boldsymbol{I}_{f_j,k}(y)$ are obtained from

$$\boldsymbol{I}_{f_j,k}(y) = \sum_{x=x_1}^{x_2} \hat{\boldsymbol{\psi}}_{f_j}(x, y)\, \mathrm{e}^{-\mathrm{i}kx}, \tag{2.5}$$

where k is the axial wavenumber, and $i = \sqrt{-1}$. In order to analyse the different components of the acoustic feedback loop further, bandpass wavenumber filters are applied. The wave structures $\tilde{\boldsymbol{\psi}}_{f_j,[k_1,k_2]}(x, y)$ within the axial wavenumber domain $[k_1, k_2]$ are reconstructed via

$$\tilde{\boldsymbol{\psi}}_{f_j,[k_1,k_2]}(x, y) = \sum_{k=k_1}^{k_2} \boldsymbol{I}_{f_j,k}(y)\, \mathrm{e}^{\mathrm{i}kx}. \tag{2.6}$$

3. Results and discussions

3.1. *Results of acoustic measurements and schlieren visualizations*

The acoustic measurements in the present study are not conducted in an anechoic environment. The purpose of these measurements is to obtain the frequencies of screech tones. In order to explore the influence of the inclined impinging plate on the evolutionary process of screech frequencies, acoustic measurements are conducted on underexpanded free jets and the underexpanded jets that impinge on an inclined plate. The results of the acoustic experiments are presented in figure 2. As shown in figure 2(*a*), with the increase of M_j, the screech frequencies of free jets exhibit several typical stages, and the tonal frequencies of impinging jets are also divided into similar stages in figure 2(*b*). However, there are some differences in the mode staging processes of the axisymmetric screech modes between free and impinging jets. The M_j range for the A2 screech mode of impinging jets is obviously wider than that of underexpanded free jets. For underexpanded free jets, the screech mode transforms from the A2 mode to the B mode around $M_j = 1.19$

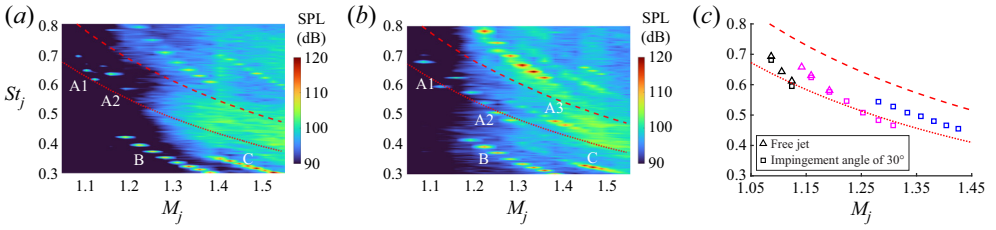

Figure 2. Contour of the sound pressure level (SPL) as a function of M_j for (*a*) underexpanded free jets, and (*b*) impinging jets. Here, $St_j = fD_j/U_j$, where f is the frequency, D_j is the ideally expanded equivalent jet diameter, and U_j is the ideally expanded velocity. The screech frequencies of axisymmetric modes in (*a*,*b*) are extracted and plotted in (*c*). The black, magenta and blue symbols in (*c*) indicate the A1, A2 and A3 screech modes, respectively. Dotted and dashed red lines, respectively, correspond to the branch- and saddle-point tracks of the (0, 2) upstream-propagating guided jet mode (Tam & Ahuja 1990).

(NPR = 2.40), which agrees with our previous results (Li *et al.* 2021). As shown in figure 2(*b*), the impinging jets generate strong tones that belong to the A2 mode until $M_j = 1.28$ (NPR = 2.70). When M_j is around 1.36 (NPR $\approx$ 3.0), the dominant screech mode of free jets is the flapping B mode or the helical C mode. In figure 2(*b*), from $M_j = 1.28$ to $M_j = 1.45$, there are evident tones of impinging jets in the frequency range where the axisymmetric upstream-propagating guided jet mode (0, 2) (Tam & Ahuja 1990) is propagable. In the following subsections, the analysis results of schlieren data will indicate that the azimuthal feature of the dominant flow structures at these tonal frequencies is axisymmetric. This screech mode is denoted as A3 in the present paper. The tonal frequencies belonging to the axisymmetric screech modes of free and impinging jets are extracted from figures 2(*a*) and 2(*b*), and compared with each other in figure 2(*c*). At the same M_j, the screech frequency of free jets agrees well with that of impinging jets.

Based on the above-mentioned acoustic results, three flow conditions, $M_j = 1.12$, 1.28 and 1.40, are chosen to investigate the acoustic resonance mechanism of the A1, A2 and A3 screech modes for the underexpanded jets that impinge on an inclined plate. The schlieren snapshots of the impinging jets at these three Mach numbers are shown in figure 3, and the schlieren snapshots of the free jets at the same M_j are also plotted as a reference. The nozzle exit is located at $X/D = 0$. In these schlieren images, negative density gradients in the jet axial direction appear as the brighter regions, such as the expansion fan near the nozzle exit, and positive density gradients in the jet direction correspond to the darker regions, such as the shocks in the jet core. Along the jet shear layer, the successive bright and dark regions are respectively associated with the expansion and compression parts of the K–H wavepacket. At $M_j = 1.12$, both the free and impinging jets generate the screech tones of the axisymmetric A1 mode. As shown in figures 3(*a*,*d*), in the axial range of the first several shock cells, the dominant instability waves of the free and impinging jets are nearly symmetric with respect to the jet axis. For the free jets, the dominant screech mode is the B mode at $M_j = 1.28$, and transforms from the B mode to the C mode at $M_j = 1.40$. The instability waves in the upper and lower sides of the free jets are out of phase in figures 3(*b*,*e*) and 3(*c*,*f*). As shown in figure 2(*b*), at $M_j = 1.28$ and 1.40, the impinging jets generate multiple tones that respectively belong to the axisymmetric and antisymmetric modes. Thus the features of instability waves in the shear layers of impinging jets are more complex, as presented in figures 3(*b*,*e*) and 3(*c*,*f*).

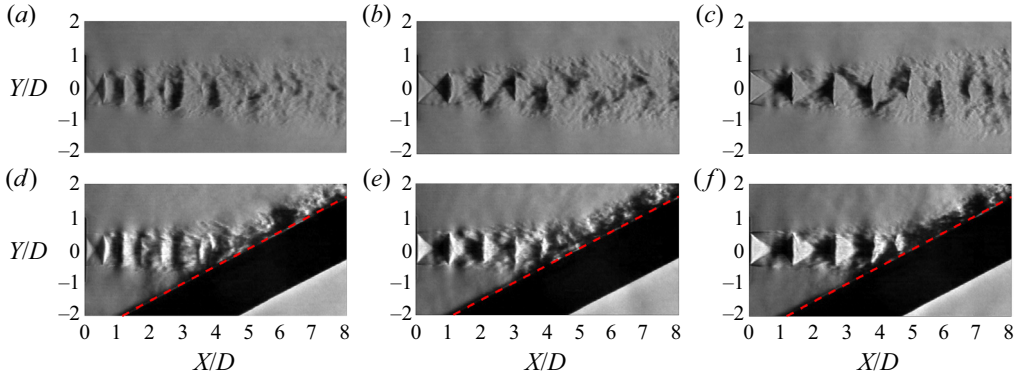

Figure 3. Schlieren snapshots of (*a–c*) underexpanded free jets, and (*d–f*) impinging jets, at (*a*,*d*) $M_j = 1.12$, (*b*,*e*) $M_j = 1.28$, and (*c*,*f*) $M_j = 1.40$.

3.2. *Characteristics of averaged shock structures*

As shown in figure 3, underexpanded jets impinge on the inclined plate, and downstream of the impingement location, the deflected jet turns into a wall jet (Brehm *et al.* 2016). Previous experiments of André, Castelain & Bailly (2014) determined that the potential core length of an underexpanded free jet is approximately $9D$, and the potential core becomes longer with the increase of M_j. In the current experimental configuration, the jet impingement occurs before the end of the potential core. Thus the inclined plate can influence the shock cell structures to some extent.

Integrated spatial characteristics of shock cell structures are required to explain the staging behaviour of screeching free jets (Edgington-Mitchell *et al.* 2022; Nogueira *et al.* 2022*a*). Therefore, the averaged shock structures in the underexpanded jets impinging on an inclined plate are analysed in detail. The averaged schlieren images of the underexpanded impinging jets at $M_j = 1.12$, 1.28 and 1.40 are shown in figure 4, and the averaged schlieren images of their free counterparts are also displayed as a reference. These averaged schlieren images are obtained by using 2560 successive schlieren images. Hundreds of screech periods are contained in this duration. The averaged greyscale distributions along $Y/D = 0$, and their wavenumber spectra, are also presented in figure 4 to better demonstrate the similarities and differences between averaged shock structures in underexpanded free and impinging jets. The streamwise domain of spatial Fourier transforms for impinging jets is $0 \leqslant X/D \leqslant 6$. For underexpanded free jets, the axial fluctuations of greyscales associated with shock cells are almost invisible at $10D$ downstream of the nozzle exit. The streamwise domains for spatial transforms of free jets are respectively set as $0 \leqslant X/D \leqslant 10$ and $0 \leqslant X/D \leqslant 6$, to analyse the effect of the domain lengths on the shock wavenumber spectra.

The wavenumber spectra of underexpanded free and impinging jets that are shown in figure 4 have similar features. There is a primary peak in each wavenumber spectrum that is associated with the first several shock cells whose shock spacings are relatively constant. On the right of this primary peak, a series of suboptimal peaks represent the axial variation in shock spacing that occurs further downstream (Edgington-Mitchell *et al.* 2022). The primary shock wavenumber peak is denoted as k_{s1} and is indicated by the red squares in figure 4; the first and second suboptimal shock wavenumber peaks are denoted as k_{s2} and k_{s3}, indicated by the magenta and cyan squares, respectively. As shown in figure 4, the spacings of the first several shock cells of impinging jets have good agreement with

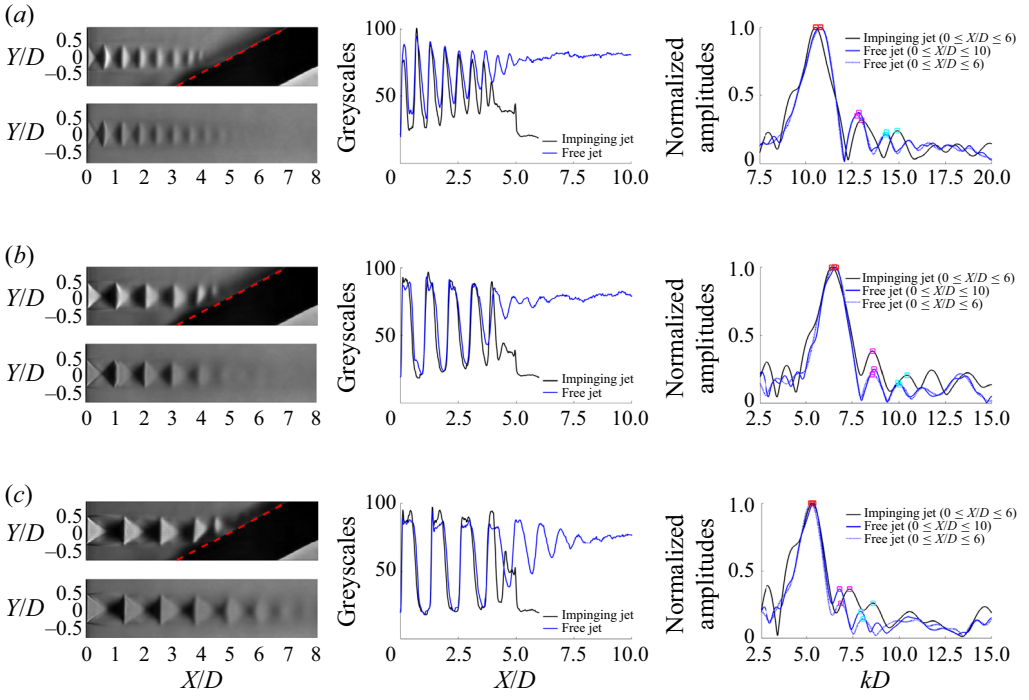

Figure 4. Averaged schlieren images, distributions and wavenumber spectra of averaged greyscales along $Y/D = 0$ of underexpanded free and impinging jets at (*a*) $M_j = 1.12$, (*b*) $M_j = 1.28$, and (*c*) $M_j = 1.40$. The primary shock wavenumber peak k_{s1} is indicated by the red square. The first and second suboptimal shock wavenumber peaks (k_{s2} and k_{s3}) are respectively indicated by the magenta and cyan squares.

those of the corresponding free jets. Thus the k_{s1} values of impinging jets are very close to those of the corresponding free jets. However, the shock cells of impinging jets, which are located just upstream of the impinging plate, are obviously shorter. By comparing with the corresponding free jets, the sixth and seventh shock cells of the $M_j = 1.12$ impinging jet, the fifth shock cell of the $M_j = 1.28$ impinging jet, and the fourth shock cell of the $M_j = 1.40$ impinging jet have shorter spacings. The axial variation of shock spacings of impinging jets is more drastic because of the existence of the impinging plate. Correspondingly, at $M_j = 1.12$ and 1.28, the k_{s2} values of impinging and free jets are very close to each other, and the k_{s3} values of impinging jets have higher wavenumbers. In the case $M_j = 1.40$, the wavenumbers of both k_{s2} and k_{s3} of the impinging jet are higher than those of the corresponding free jet. It is indicated that the effect of the impinging plate on jet shock cell structures becomes more obvious with the increase of M_j. Furthermore, in each case of figure 4, the peaks in the wavenumber spectra of the free jet based on different domain lengths are close to each other. This implies that the influence of domain lengths for spatial Fourier transforms on the shock spectra of free jets is limited, and the above-mentioned differences in the shock wavenumber spectra between the free and impinging jets are not due to the different domain lengths.

In order to analyse the sensitivities of k_{s1}, k_{s2} and k_{s3} to the choice of radial position, spatial Fourier transforms are conducted at different radial positions, and the resultant wavenumber spectra are represented in figure 5. As shown in figure 4, the averaged shock structures of free jets are symmetric with respect to the jet axis. The high-amplitude regions corresponding to k_{s1}, k_{s2} and k_{s3} in the shock wavenumber spectra of free jets

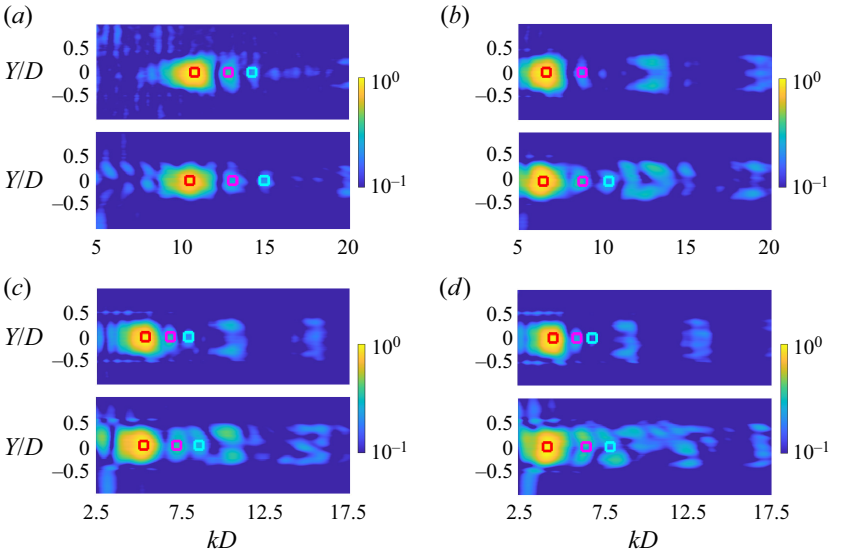

Figure 5. Normalized wavenumber spectra of averaged schlieren images for underexpanded free and impinging jets at (*a*) $M_j = 1.12$, (*b*) $M_j = 1.28$, (*c*) $M_j = 1.40$, and (*d*) $M_j = 1.51$. In each panel, the top image is the spectrum of the free jet and the bottom image is the spectrum of the impinging jet. The primary shock wavenumber peak k_{s1} is indicated by the red square. The first and second suboptimal shock wavenumber peaks (k_{s2} and k_{s3}) are respectively indicated by the magenta and cyan squares.

are concentrated mainly at the jet axis, as displayed in figure 5. Thus the determinations of the peak wavenumbers of averaged shock cells for free jets are based on the wavenumber spectra along $Y/D = 0$. For impinging jets, as shown in figure 5, the high-amplitude regions corresponding to k_{s1} and k_{s2} are also located mainly at the jet axis. The k_{s3} values can still be determined at the jet axis in figures 5(*a*), 5(*b*) and 5(*c*). However, for the impinging jet at $M_j = 1.51$, there are two spots of higher amplitudes near $Y/D = \pm 0.25D$ on the right of the k_{s2}, as shown in figure 5(*d*). This is because of the asymmetry of averaged shock structures under the influence of the inclined impinging plate at higher M_j. In view of the approximate wavenumbers of these two high-amplitude spots, k_{s3} is defined as the average of the wavenumbers corresponding to the maximum amplitude points of these two spots for these cases, to represent the axial variation in shock spacing.

The full spectrum representations of averaged shock structures for underexpanded free and impinging jets are displayed in figures 6(*a*) and 6(*b*), respectively. The range of M_j is from 1.09 to 1.56. The wavenumber spectra of 20 cases are displayed in each figure. The wavenumber spectrum in $-0.5 \leqslant Y/D \leqslant 0.5$ of the time-averaged schlieren image is plotted for each case. Nogueira *et al.* (2022*a*) suggested that the A1 and A2 screech modes are respectively closed by the guided jet modes that are energized by the interaction between the K–H wavepacket and the first two shock wavenumber peaks. The k_{s1} and k_{s2} values of free and impinging jets are extracted from figures 6(*a*) and 6(*b*), and are compared in figure 6(*c*). In the present M_j range, the k_{s1} value of impinging jets has good agreement with that of free jets, and the specific values of k_{s2} of impinging jets are slightly higher than those of free jets at some M_j. The k_{s3} value is more noticeable in figure 6(*b*). For the shock wavenumber of impinging jets, k_{s3} corresponds to the change of shock cell spacings caused by the appearance of the impinging plate. The values of k_{s3} for impinging jets are also extracted from figure 6(*b*) and displayed in figure 6(*c*) for further research.

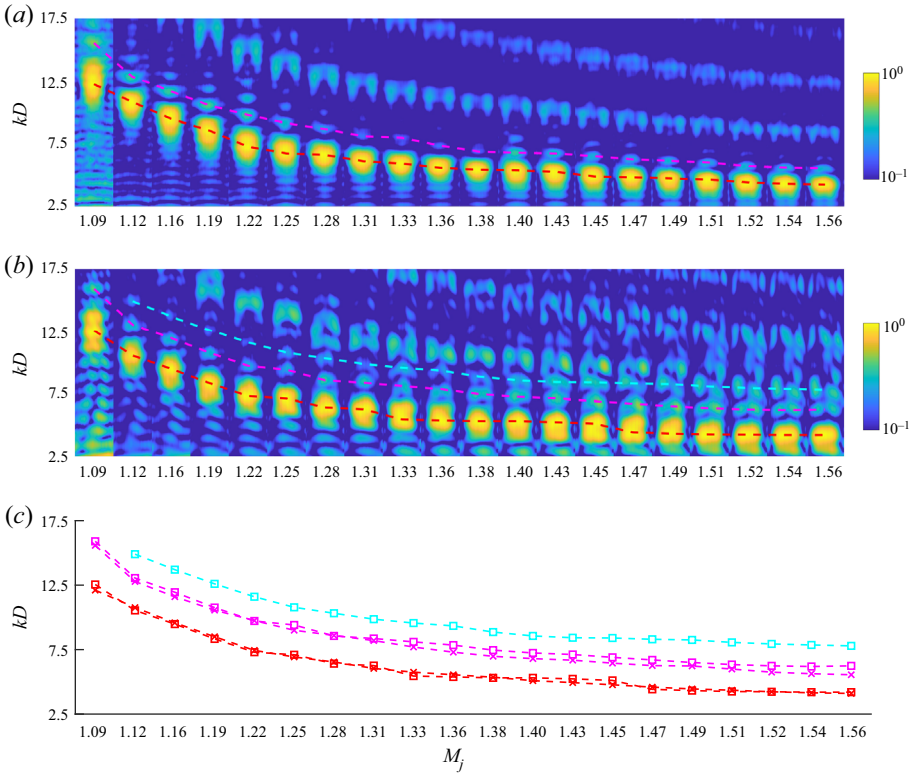

Figure 6. Normalized wavenumber spectra of averaged schlieren images as a function of M_j for (*a*) underexpanded free jets and (*b*) impinging jets. The red, magenta and cyan dashed lines respectively display the trends of k_{s1}, k_{s2} and k_{s3}. The k_{s1}, k_{s2} and k_{s3} values of underexpanded free and impinging jets are extracted from (*a*,*b*) and plotted in (*c*). The shock wavenumbers of free and impinging jets are respectively indicated by the crosses and squares in (*c*). The red, magenta and cyan symbols in (*c*) are respectively corresponded to k_{s1}, k_{s2} and k_{s3}.

3.3. *Eigenvalues and modes of SPOD*

SPOD is applied on the schlieren image sequences in order to obtain the coherent flow structures that are associated with the generation of screech tones. In the present analyses, $M = 2560$ snapshots are used in each case. For the current M_j range, with the increase of M_j, the non-dimensional time step between consecutive snapshots $\Delta t\, U_j/D_j$ ranges from 0.42 to 0.50. The range of the corresponding maximum resolvable non-dimensional frequency is from 1.19 to 1.00. Here, N_f (size of each block) and N_o (overlap between two consecutive blocks) are respectively set as 256 and 128 ($0.5N_f$), resulting in a total of $N_b = 19$ SPOD modes at each frequency. The non-dimensional frequencies St_j of the acoustic resonances that are investigated in the following subsections are in the range 0.40 to 0.70. The non-dimensional time span of one block is more than 100, which corresponds to tens of periods of acoustic resonance.

As shown in figure 7, for the impinging jets at $M_j = 1.12$, 1.28 and 1.40, the tonal frequencies of the noise spectra agree well with the peak frequencies in the distributions of the eigenvalues of the first SPOD modes; and at tonal frequencies, the first SPOD modes are obviously more energetic than the second and third SPOD modes. These results indicate that the flow structures at tonal frequencies possess more energy and show

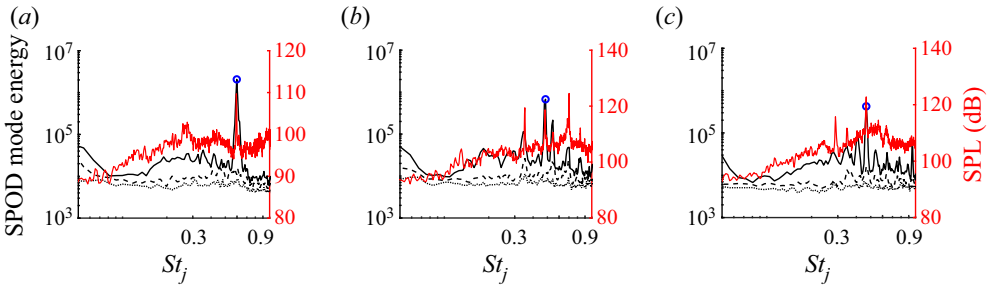

Figure 7. SPOD energy spectra and acoustic spectra for the impinging jets at (*a*) $M_j = 1.12$, (*b*) $M_j = 1.28$, and (*c*) $M_j = 1.40$. The black solid, dashed and dotted lines respectively indicate the SPOD eigenvalues of the first three SPOD modes. The red lines indicate the noise spectra. The blue circles indicate the chosen SPOD modes.

M_j	NPR	Screech mode	St_j (acoustic measurements)	St_j (SPOD modes)
1.12	2.20	A1	0.59	0.60
1.28	2.70	A2	0.48	0.49
1.40	3.20	A3	0.47	0.47

Table 1. Frequencies of screech tones and chosen SPOD modes for different jets.

a low-rank dynamic feature. Therefore, in the following subsections, the structures of screech feedback loops are investigated based mainly on the first SPOD modes at tonal frequencies. As shown in figure 2(*b*), the impinging jets at $M_j = 1.12$, 1.28 and 1.40 generate the screech tones of the A1, A2 and A3 modes, respectively. The frequencies of the chosen SPOD modes are indicated by blue circles in figure 7, and summarized in table 1.

As presented in figure 8, upstream of the impingement location, the real parts of the chosen SPOD modes are symmetric with respect to the jet axis, which agrees with the azimuthal feature of the A1 and A2 modes, and indicates that the A3 mode is another kind of axisymmetric screech mode. In figure 8, the normalized amplitude fields of the chosen SPOD modes exhibit standing wave patterns (Panda 1999; Edgington-Mitchell 2019) along the jet shear layer. The presence of this standing wave pattern is due to the partial interference between the upstream- and downstream-propagating waves that constitute the screech feedback loop (Panda 1999). Moreover, as presented in figures 8(*c*,*f*), the amplitudes on the lower side of the jet are slightly weaker than those on the jet's upper side. This phenomenon will be discussed further in the following subsections.

3.4. *Wavenumber spectra of SPOD modes*

In a chosen SPOD mode, the flow structures oscillate at a specific screech frequency. However, the different components of the screech feedback loop are associated with a broad range of wavenumbers. Thus spatial Fourier transforms are conducted on the chosen SPOD modes using (2.5). The axial range for the spatial Fourier transform is from $X/D = 0$ to $X/D = 8$. The normalized wavenumber spectra of the current three SPOD modes are presented in figure 9. In the positive wavenumber domain, the majority of energy is associated with the downstream-propagating K–H wavepacket. The wavenumber

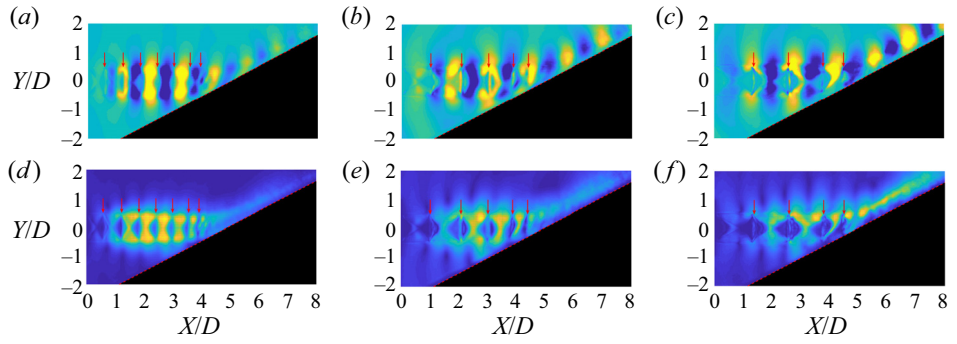

Figure 8. The first SPOD modes for jets with (*a*,*d*) $M_j = 1.12$ at $St_j = 0.60$, (*b*,*e*) $M_j = 1.28$ at $St_j = 0.49$, and (*c*,*f*) $M_j = 1.40$ at $St_j = 0.47$. (*a–c*) Real part of the mode. The blue contours indicate negative values, and yellow contours indicate positive values. (*d–f*) Normalized amplitude field of the mode. The colour scales range from 0 (blue) to 1 (yellow).

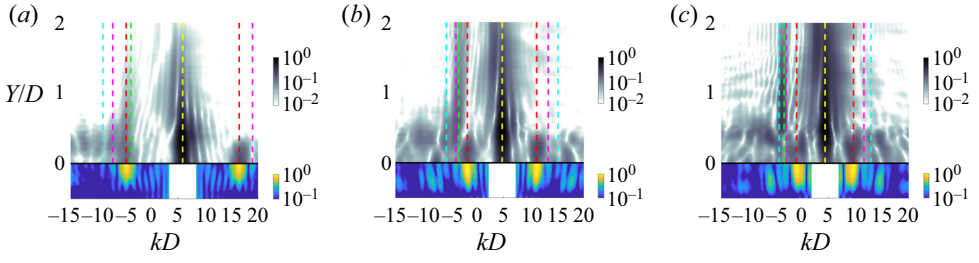

Figure 9. Normalized wavenumber spectra of the chosen SPOD modes for the jets at (*a*) $M_j = 1.12$, (*b*) $M_j = 1.28$, and (*c*) $M_j = 1.40$. The dashed vertical yellow lines indicate the wavenumber of k_h. The dashed vertical red, magenta and cyan lines respectively indicate the wavenumbers of $k_h \pm k_{s1}$, $k_h \pm k_{s2}$ and $k_h \pm k_{s3}$. The dashed vertical green lines indicate the wavenumber of the upstream-propagating acoustic wave $k_a = -\omega_s/a_\infty$. The $k_h\pm$ spectrum of the averaged schlieren image is also shown in the bottom of each panel as a reference.

of the K–H wavepacket (k_h), which is estimated as the wavenumber corresponding to the maximum amplitude in the positive wavenumber domain, is indicated by the yellow dashed lines in figure 9 and listed in table 2. Then the convective velocity of the K–H wavepacket is calculated as $U_c = \omega_s/k_h$, where ω_s is the angle frequency of screech. As shown in table 2, the U_c value for the chosen cases ranges from $0.60U_j$ to $0.65U_j$, which agrees with the results in Mercier, Castelain & Bailly (2017) and Powell *et al.* (1992).

At screech frequencies, the upstream-propagating guided jet mode can be stimulated by the interaction between the K–H wavepacket and shock cell structures (Edgington-Mitchell *et al.* 2021*a*); Nogueira *et al.* (2022*a*) suggested that the A1 and A2 screech modes are respectively closed by the guided jet modes that are energized by the interaction between the k_h and different shock wavenumbers. Thus, for the present three cases, $k_h\pm$, the spectrum of the averaged schlieren image, is also plotted in figure 9. It should be noted that there are some high-amplitude regions that are located mainly in the lower wavenumber domains in the wavenumber spectra of averaged schlieren images. The wavenumbers of these high-amplitude regions are obviously less than k_{s1} and may correspond to the nozzle-to-plate distance. The low-wavenumber domains of the wavenumber spectra of averaged schlieren images are omitted in figure 9, which leads to the white gaps in figure 9. The wavenumbers of high-amplitude regions in the wavenumber spectra of SPOD modes

M_j	NPR	k_hD	U_c/U_j	$k_hD-k_{s1}D$	$k_hD-k_{s2}D$	$k_hD-k_{s2}D$	k_aD
1.12	2.20	5.92	0.63	−4.64	−7.13	−8.98	−3.75
1.28	2.70	4.74	0.63	−1.67	−3.82	−5.58	−3.30
1.40	3.20	4.35	0.64	−0.95	−2.89	−4.21	−3.29

Table 2. Characteristic wavenumbers in the wavenumber spectra of SPOD modes.

have good agreement with $k_h \pm k_{s1}$, $k_h \pm k_{s2}$ and $k_h \pm k_{s3}$. These results suggest that the interactions between the K–H wavepacket and the shock cells distribute energy to all of these wavenumbers. However, the radial features of the jet modes corresponding to these energetic wavenumbers are different. In the positive wavenumber domain, the stimulated waves at $k_h + k_s$ are trapped mainly in the jet core. These are the duct-like modes that are identified by Edgington-Mitchell *et al.* (2021*a*) via local stability analyses, and are similar to that identified in high-subsonic jets (Towne *et al.* 2017). For the case $M_j = 1.12$, there is more energy at $k_h - k_{s1}$, $k_h - k_{s2}$ and $k_h - k_{s3}$ in the negative wavenumber domain. At the first interaction wavenumber, there are significant supports outside the shear layer, which agrees with the radial feature of the upstream-propagating guided jet mode (Tam & Ahuja 1990), while at the latter two wavenumbers, the energy decays rapidly in the radial direction. This implies that the stimulated wave at $k_h - k_{s1}$ is the upstream-propagating guided jet mode, and the waves at $k_h - k_{s2}$ and $k_h - k_{s3}$ would be duct-like. At $M_j = 1.28$ and 1.40, the energies associated with $k_h - k_{s2}$ and $k_h - k_{s3}$ are respectively no longer trapped within the jet core and have supports outside the jet shear layer. This indicates that at the screech frequencies of the A2 and A3 modes, the upstream-propagating guided jet modes are respectively energized by the interactions between the K–H wavepacket and the first and second suboptimal shock wavenumber peaks. Thus the present results support the conclusion of Nogueira *et al.* (2022*a*) and indicate that the A3 screech mode of impinging jets is related to the interaction between k_h and the k_{s3}. As discussed in previous subsections, k_{s3} is associated with the change of shock cell spacings that is caused by the impinging plate. The external boundaries, such as the impinging plate, can affect the screech mode of jets by changing the axial sizes of shock cells.

In order to generalize the conclusions of figure 9, SPOD is conducted on the schlieren image sequences of the cases in the M_j range from 1.09 to 1.43. Spatial Fourier transforms are conducted on the first SPOD modes at tonal frequencies of different axisymmetric screech modes. The wavenumber spectrum $Y/D \subseteq [0, 1]$ for each case is shown in figure 10. Overall, the results of figure 9 are further confirmed by the wavenumber spectra that are displayed in figure 10. The acoustic resonances of the A1, A2 and A3 screech modes are respectively attributed to the interactions between the K–H wavepacket and the shock wavenumbers k_{s1}, k_{s2} and k_{s3}.

Shock cell spacings (Powell 1953) and standing wave wavelengths (Panda 1999) are both important length scales for predicting screech frequencies. The relationship between these two length scales was discussed in Mercier *et al.* (2017) and Li *et al.* (2021). Here, the connection between these two length scales is analysed via the wavenumber spectra of the normalized amplitude fields of the chosen SPOD modes. As shown in figures 9 and 10, the upstream-propagating guided jet modes with the wavenumbers of $k_h - k_{s1}$, $k_h - k_{s2}$ and $k_h - k_{s3}$, respectively, close the screech feedback loops of the A1, A2 and A3 modes. Based on the wavenumber relation of the standing wave, the standing wave patterns with the wavenumbers of k_{s1}, k_{s2} and k_{s3} should respectively exist in the flow fields of the jets

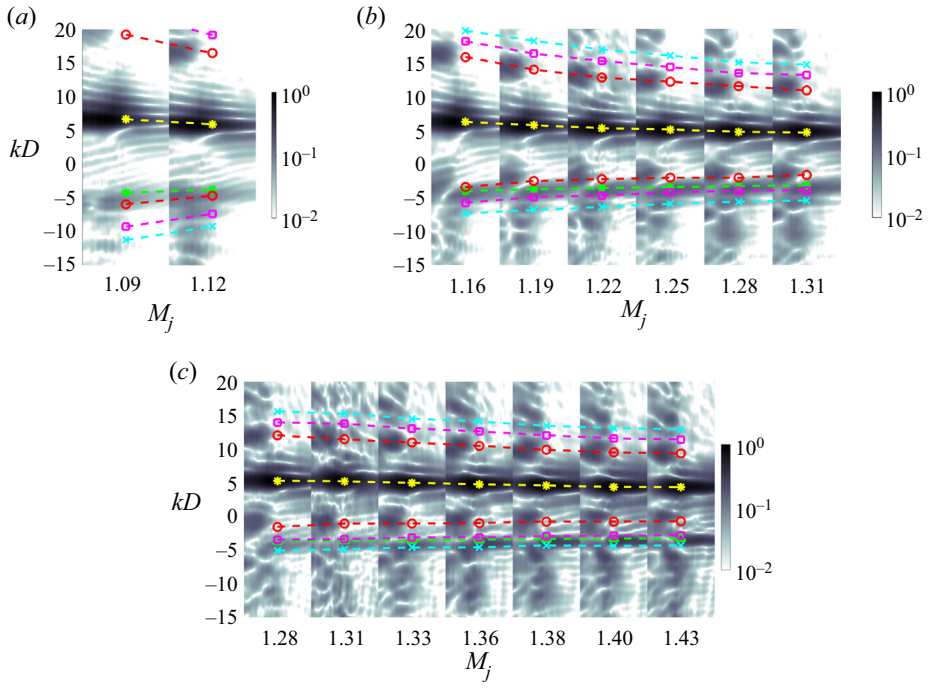

Figure 10. Normalized wavenumber spectra of the first SPOD modes at the screech frequencies of (*a*) the A1 mode, (*b*) the A2 mode, and (*c*) the A3 mode. The yellow symbols indicate the wavenumber of k_h. The red, magenta and cyan symbols respectively indicate the wavenumbers of $k_h \pm k_{s1}$, $k_h \pm k_{s2}$ and $k_h \pm k_{s3}$. The green symbols indicate the wavenumber of the upstream-propagating acoustic wave $k_a = -\omega_s/a_\infty$.

that produce the screech tones in the A1, A2 and A3 modes. Figure 11 shows that the wavenumbers of high-amplitude regions are around k_{s1}, k_{s2} and k_{s3} in the radial range $0 \leqslant Y/D \leqslant 0.5$. In the study of Panda (1999), the wavenumber of standing wave k_{sw} is considered as $k_h - k_a$. For the A1, A2 and A3 modes, during the process of getting away from the jet axis, the high-amplitude regions corresponding to k_{s1}, k_{s2} and k_{s3} approach $k_h - k_a$, respectively. In different screech modes, the axial wavenumber of the standing wave pattern corresponds to the different wavenumber peaks of averaged shock structures. As shown in figure 8, the corresponding relationships between the shock cell spacings and standing wave wavelengths are different in the A1, A2 and A3 modes. In the axial range of the first three shock cells, there are nearly three anti-nodes of the standing wave pattern for the A1 mode, four anti-nodes for the A2 mode, and five anti-nodes for the A3 mode. The above results will be used to predict the screech frequencies in the following subsections.

3.5. *Mode staging process of axisymmetric screech modes*

The weakest link theory (Tam & Tanna 1982; Tam, Seiner & Yu 1986) suggested that the interaction between the K–H wavepacket and shock cells leads to a redistribution of energy. The waves with the wavenumbers of the sum and difference of k_h and k_s will be energized. At screech frequencies, the wavenumbers of upstream-propagating guided jet modes coincide with these interaction wavenumbers, i.e. $k_h - k_s$ (Edgington-Mitchell *et al.* 2021*a*). The weakest link theory can be viewed as a first approximation of the condition for the occurrence of the absolute instability (Nogueira *et al.* 2022*a*,*b*). Here, the mode staging process of the axisymmetric screech modes for the impinging jets is analysed

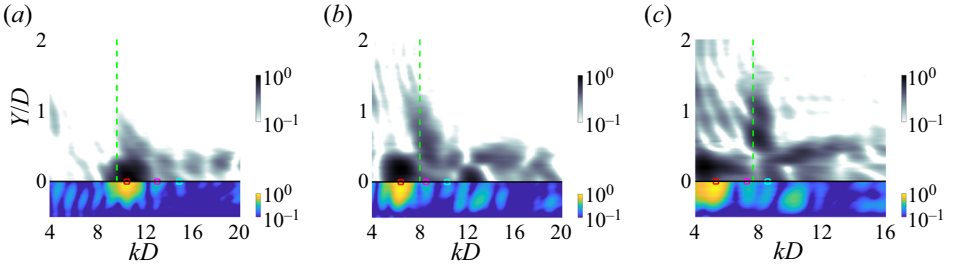

Figure 11. Normalized wavenumber spectra for the amplitude fields of the chosen SPOD modes for the jets at (*a*) $M_j = 1.12$, (*b*) $M_j = 1.28$, and (*c*) $M_j = 1.40$. The spectrum of the averaged schlieren image is also shown at the bottom of each panel as a reference. The dashed vertical green lines indicate the wavenumber of $k_h - k_a$.

by combining the weakest link theory and the dispersion relations of upstream-propagating guided jet modes.

The dispersion relation of the vortex sheet model (Lessen, Fox & Zien 1965; Tam & Hu 1989) can be written as

$$\frac{1}{\left(1-\dfrac{kM_a}{\omega}\right)^2}+\frac{1}{T}\frac{I_m\left(\dfrac{\gamma_i}{2}\right)\left[\dfrac{\gamma_o}{2}K_{m-1}\left(\dfrac{\gamma_o}{2}\right)+mK_m\left(\dfrac{\gamma_o}{2}\right)\right]}{K_m\left(\dfrac{\gamma_o}{2}\right)\left[\dfrac{\gamma_i}{2}I_{m-1}\left(\dfrac{\gamma_i}{2}\right)+mI_m\left(\dfrac{\gamma_i}{2}\right)\right]}=0 \tag{3.1}$$

and

$$\gamma_i=\sqrt{k^2-\frac{1}{T}(\omega-M_ak)^2}, \tag{3.2}$$

$$\gamma_o=\sqrt{k^2-\omega^2}. \tag{3.3}$$

Here, I_m and K_m are modified Bessel functions of the first and second kinds, respectively. All quantities have been normalized by the ideally expanded jet diameter D_j and the ambient sound velocity a_∞. Also, $M_a = U_j/a_\infty$ is the acoustic Mach number, and $T = T_j/T_\infty$ is the temperature ratio. The relation between the ideally expanded jet Mach number M_j and the acoustic Mach number M_a is $M_j = M_a/\sqrt{T}$. For given values of wavenumber k and azimuthal wavenumber m, the dispersion relation (3.1) has many real roots or eigenvalues. The entire set of eigenvalues can be characterized by m and a radial wavenumber n (Tam & Ahuja 1990). For convenience, the jet mode that corresponds to the mth azimuthal mode and the nth radial mode will be designated by (m, n), where $m = 0, 1, 2, \ldots$ and $n = 1, 2, 3, \ldots$. The pressure eigenfunctions of guided jet modes are given by

$$p_i = I_0(\gamma_i r)(0 \leqslant r/D_j \leqslant 0.5), \quad p_o = A\,K_0(\gamma_o r)(0 \leqslant r/D_j \leqslant 0.5). \tag{3.4a,b}$$

These two functions are matched at $r/D_j = 0.5$ by the coefficient A.

The dispersion relations of the guided jet modes $(0, 2)$ for the cases associated with the staging process from the A1 mode to the A2 mode are shown in figure 12. The wavenumbers energized by the interaction between the K–H wavepacket and shock cells, i.e. $k_h - k_{s1}$ (red dashed lines) and $k_h - k_{s2}$ (magenta dashed lines), are also displayed. Here, the K–H waves are assumed to be non-dispersive waves with the phase velocities that are listed in table 2 for different screech modes. As shown in figure 12(*a*), the red dashed line intersects the dispersion relation of the $(0, 2)$ mode, and the frequency of

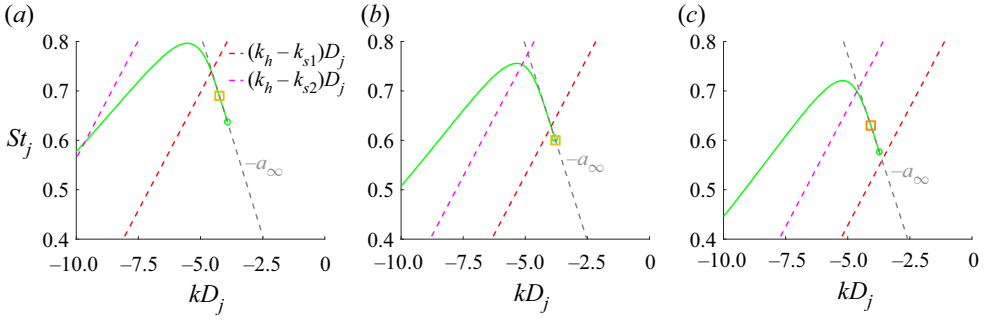

Figure 12. Dispersion relations of the upstream-propagating guided jet modes (0, 2) (green lines) for the jets at (*a*) $M_j = 1.09$, (*b*) $M_j = 1.12$, and (*c*) $M_j = 1.16$. The red and magenta dashed lines respectively indicate the wavenumbers of $k_h - k_{s1}$ and $k_h - k_{s2}$. The wavenumber of acoustic waves is represented by the grey dashed line. The yellow and orange squares respectively indicate the screech frequencies of the A1 and A2 modes.

this intersection ($St_j = 0.73$) is just above the screech frequency of the $M_j = 1.09$ jet ($St_j = 0.69$). The guided jet mode that is energized by the interaction between the K–H wavepacket and the dominant shock wavenumber of k_{s1} closes the screech feedback loop of the A1 mode (Nogueira *et al.* 2022*a*). For this M_j, no intersection is found for the magenta dashed line with the upstream-propagating part of the dispersion relation. This implies that at this condition, $k_h - k_{s2}$ does not correspond to an upstream-propagating mode that is supported by the jet. The values of k_{s1} and k_{s2} decrease with the increase of M_j. As shown in figure 12(*b*), the red dashed line intersects the upstream branch of the dispersion relation near the cut-on frequency of the guided jet mode, and the intersection point of the magenta dashed line and the dispersion relation gradually moves to the upstream branch. When $M_j = 1.16$, as shown in figure 12(*c*), there is no intersection between the red dashed line and the dispersion relation of the (0, 2) mode, which means that $k_h - k_{s1}$ does not correspond to an upstream-propagating guided jet mode. The dominant screech frequency of the $M_j = 1.16$ jet is in the A2 mode and below the frequency of the intersection of the magenta dashed line and the dispersion relation. This result agrees with that of Nogueira *et al.* (2022*a*) and indicates that the A2 mode is closed by the guided jet mode that is stimulated by the interaction between the K–H wavepacket and k_{s2} (Nogueira *et al.* 2022*a*).

We examine the characteristics of the guided jet modes that are energized by the interactions between the K–H wavepacket and k_{s2} during the mode staging process from the A1 mode to the A2 mode. Here, $k_h - k_{s2}$ intersects the dispersion relation of the (0, 2) mode at $(St_j, kD_j) = (0.59, -9.77)$ in figure 12(*a*). As shown in figure 13(*a*), the pressure eigenfunction of this guided jet mode is mainly trapped in the jet core. Therefore, for the $M_j = 1.09$ jet, a duct-like mode with a positive group velocity but negative phase velocity is energized by the interaction between the K–H wavepacket and k_{s2}, and because of the positive group velocity, this jet mode is unable to close the resonance. As shown in figure 12(*b*), $k_h - k_{s2}$ intersects the dispersion relation near the saddle point of the guided jet mode at $M_j = 1.12$, and the eigenfunction shows some amplitudes outside the shear layer in figure 13(*b*). In figure 12(*c*), $k_h - k_{s2}$ intersects the upstream branch of the dispersion relation at $M_j = 1.16$. Furthermore, as shown in figure 13(*c*), the eigenfunction of this jet mode has significant support outside the shear layer. With the increase of M_j, the jet mode energized by the interaction between the K–H wavepacket and k_{s2} gradually changes from a downstream-propagating duct-like mode to an upstream-propagating mode

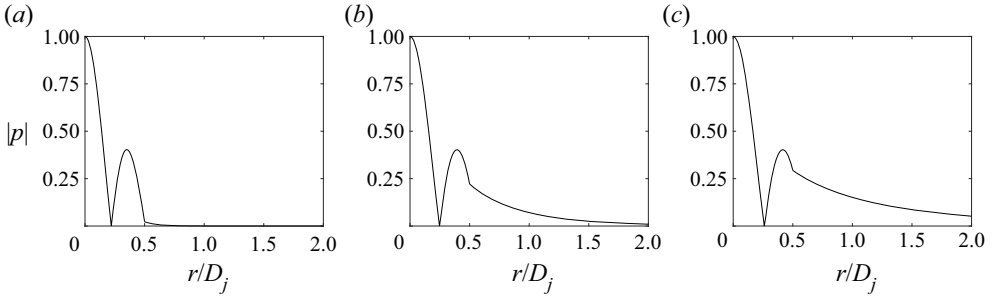

Figure 13. Pressure eigenfunction distributions of guided jet modes at the intersections of the dispersion relations of the (0, 2) mode and $k_h - k_{s2}$: (*a*) $St_j = 0.59$, $kD_j = -9.77$ for the $M_j = 1.09$ jet; (*b*) $St_j = 0.75$, $kD_j = -5.02$ for the $M_j = 1.12$ jet; and (*c*) $St_j = 0.69$, $kD_j = -4.53$ for the $M_j = 1.16$ jet.

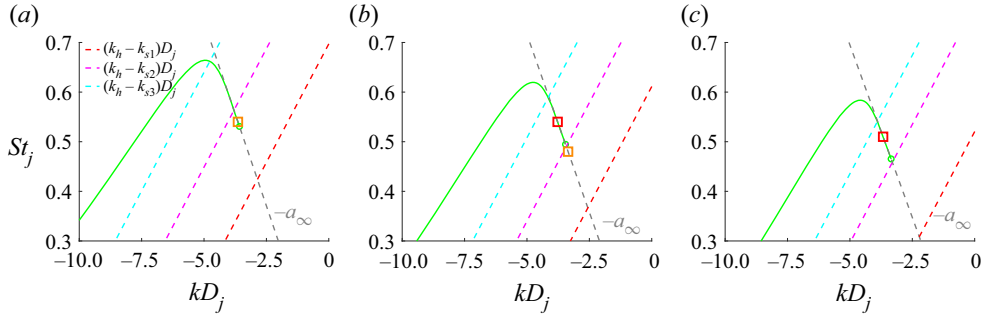

Figure 14. Wavenumbers of the upstream-propagating guided modes of the second radial order (green lines) for the jets at (*a*) $M_j = 1.22$, (*b*) $M_j = 1.28$, and (*c*) $M_j = 1.33$. The red, magenta and cyan dashed lines respectively indicate the wavenumbers of $k_h - k_{s1}$, $k_h - k_{s2}$ and $k_h - k_{s3}$. The wavenumber of acoustic waves is represented by the grey dashed line. The orange and red squares respectively indicate the screech frequencies of the A2 and A3 modes.

that has support outside the shear layer, which agrees with the results of the wavenumber spectra shown in figures 9 and 10.

The mode staging process between the A2 and A3 modes is shown in figure 14 in a similar manner to figure 12. With the increase of M_j, the line of $k_h - k_{s2}$ gradually has no intersection with the dispersion relation of the upstream-propagating guided jet mode. The screech frequency of the A3 mode is just below the frequency of the intersection of $k_h - k_{s3}$ and the upstream branch of the dispersion relation. Meanwhile, as shown in figure 15, the eigenfunctions of the jet modes energized by the interactions of the K–H wavepacket and k_{s3} gradually have more amplitudes outside the jet shear layer. These results imply further that the screech feedback loop of the A3 mode is closed by the guided jet mode that is energized by the interaction between the K–H wavepacket and k_{s3}.

As shown in figure 2, the screech frequencies of the A1 and A2 modes terminate near the cut-on frequency of the upstream-propagating guided jet mode (0, 2). However, this is not the case for the A3 mode. The acoustic results in figure 2(*b*) show that the impinging jet at $M_j = 1.47$ does not generate a strong tone of the A3 screech mode. As shown in figure 16, the line of $k_h - k_{s3}$ still intersects the upstream branch of the dispersion relation at $M_j = 1.47$. This result cannot be explained by the theory of Nogueira *et al.* (2022*a*). The termination of the A3 mode will be discussed in the following subsections.

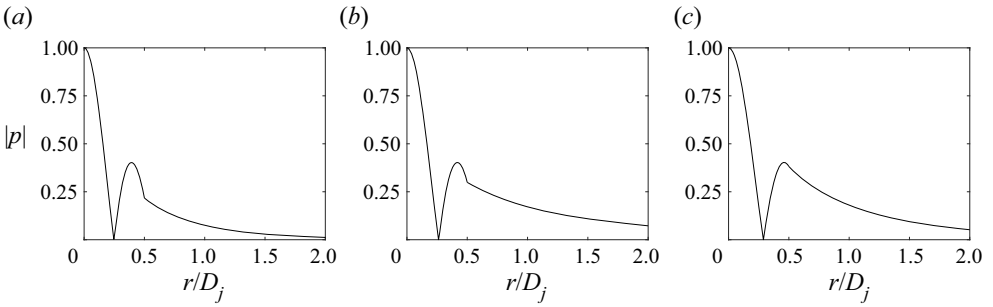

Figure 15. Pressure eigenfunction distributions of guided jet modes at the intersections of the dispersion relations of the (0, 2) mode and $k_h - k_{s3}$: (*a*) $St_j = 0.66$, $kD_j = -4.70$ for the $M_j = 1.22$ jet; (*b*) $St_j = 0.59$, $kD_j = -4.16$ for the $M_j = 1.28$ jet; and (*c*) $St_j = 0.53$, $kD_j = -3.82$ for the $M_j = 1.33$ jet.

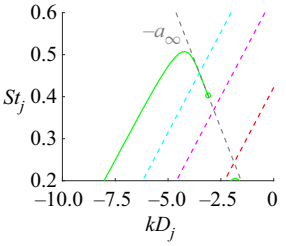

Figure 16. Wavenumbers of the upstream-propagating guided modes of the second radial order (green lines) for the $M_j = 1.47$ jet. The red, magenta and cyan dashed lines respectively indicate the wavenumbers of $k_h - k_{s1}$, $k_h - k_{s2}$ and $k_h - k_{s3}$. The wavenumber of acoustic waves is represented by the grey dashed line.

3.6. *Characteristics of upstream- and downstream-propagating waves*

The wavenumber spectra of the chosen SPOD modes are shown in figure 9. The sign of the phase velocity (ω_s/k) is determined by the sign of the axial wavenumber k. In the current analyses, in order to reconstruct the upstream- and downstream-propagating waves approximately, bandpass filters in the wavenumber domain are applied to isolate the upstream- and downstream-propagating waves in the screech feedback loop. The negative and positive wavenumber domains are used respectively to reconstruct the upstream-propagating waves and the downstream-propagating waves. The approximatively reconstructed upstream- and downstream-propagating waves at screech frequencies are presented in figure 17. Amplitude fields have been normalized by the maximum amplitude in each case for clarity. The axial locations of the rear edges of shock cells are extracted from averaged schlieren images and shown by the red arrows in figure 17.

As shown in figure 17, there are high-amplitude regions of the upstream-propagating waves at multiple shock tips for all these three screech modes. These high-amplitude regions should be related to the upstream motions of shock tips that lead to the generation of upstream-propagating acoustic waves (Edgington-Mitchell *et al.* 2021*b*). As discussed in the previous subsections, the upstream-propagating guided jet mode that is energized by the interaction of the K–H wavepacket and k_{s1} closes the screech feedback loop of the A1 mode. As shown in figure 17(*a*), some high-amplitude regions are near the impinging plate, where the shock cells are with shorter spacings. These are the energy associated mainly with the $k_h - k_{s2}$ interaction, which is also shown in the wavenumber spectrum of figure 9(*a*). In the M_j range 1.12–1.16, the screech mode transforms from the A1

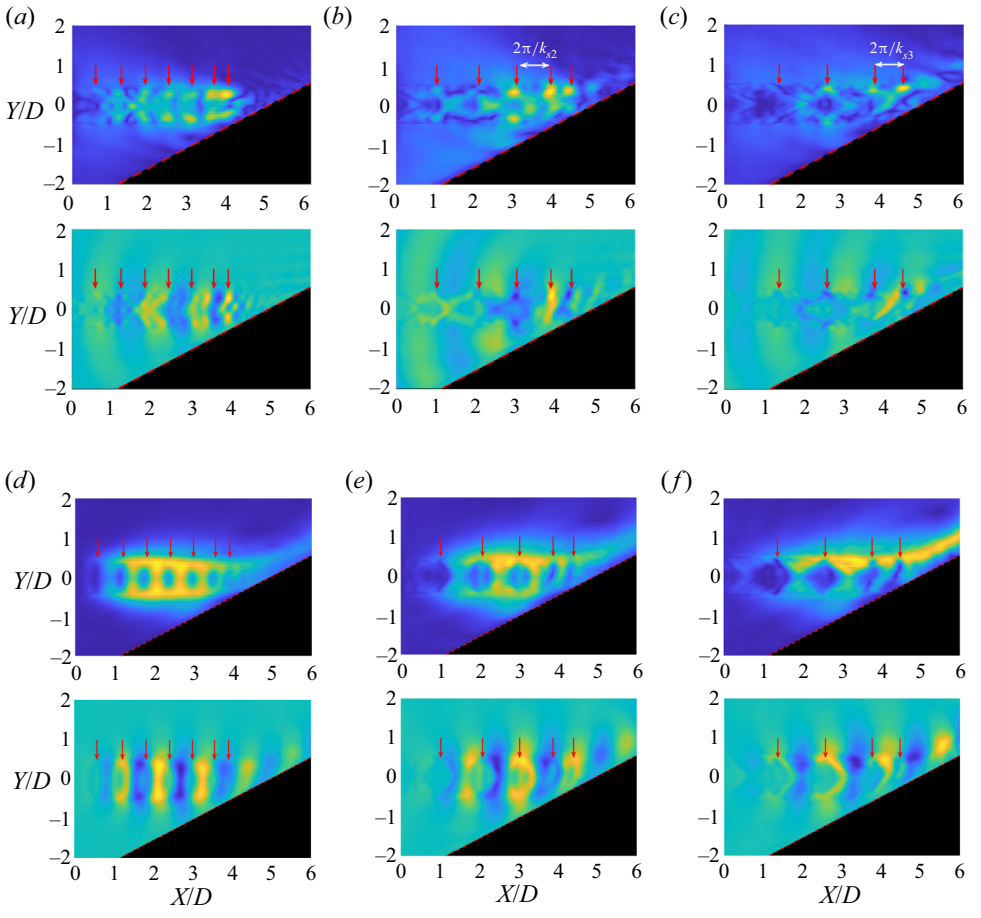

Figure 17. Approximately reconstructed upstream (*a–c*) and downstream (*d–f*) propagating waves at the screech frequencies for (*a*,*d*) the $M_j = 1.12$ jet (A1 mode), (*b*,*e*) the $M_j = 1.28$ jet (A2 mode), and (*c*,*f*) the $M_j = 1.40$ jet (A3 mode). The top image of each panel is the normalized amplitude field of waves. The colour scales range from 0 (blue) to 1 (yellow). The bottom image of each panel is the real part of the waves. Blue contours indicate negative values, and yellow contours indicate positive values. Red arrows indicate the axial positions of the shock reflection points at the jet shear layer.

mode to the A2 mode. Before the mode switch occurs, the energy associated with the interaction of the K–H wavepacket and k_{s2} becomes significant (Edgington-Mitchell *et al.* 2022). As shown in figures 17(*b*) and 17(*c*), the higher amplitudes of upstream-propagating waves in the A2 and A3 modes are concentrated mainly at the axial regions downstream of the third shock cell, where the spacings of shock cells exhibit obvious changes in the axial direction. The upstream-propagating guided jet modes that are energized by the interactions of the K–H wavepacket with k_{s2} and k_{s3} close the screech feedback loops of the A2 and A3 modes, respectively. These two shock wavenumber peaks represent the axial variations of shock spacings that occur further downstream. Thus the approximate reconstructions of upstream-propagating waves can be viewed as the spatial representations of the corresponding wavenumber spectra. The screech tones of different modes might be associated with the shock cells at different distances downstream of the jets (Edgington-Mitchell *et al.* 2022). For the A1 mode, the K–H wavepacket interacts with the first several shock cells to energize the upstream-propagating guided jet modes

that close the screech feedback loop, and the acoustic resonances of the A2 and A3 modes are associated mainly with the axial regions in which the spacings of shock cells exhibit obvious axial variations. As shown in the amplitude fields of downstream-propagating waves in figure 17, the standing wave patterns along the jet shear layer are removed. However, periodic modulations within the jet core are exhibited for all these jets. The spatial scales of these modulations match the shock cell spacings closely. These spatial modulations may be attributed to the interference between the K–H wavepacket (k_h) and the duct-like mode with the wavenumber of $k_h + k_s$ (Edgington-Mitchell *et al.* 2021*a*), or the direct modulations of shock cells on the K–H wavepacket (Nogueira *et al.* 2022*c*).

3.7. *Phase criteria*

In this subsection, the frequencies of acoustic resonances are predicted by combining the phase criterion of an acoustic feedback loop with the results of current experiments. The phase criterion can be written as (Edgington-Mitchell 2019)

$$\frac{N}{f_s} = \frac{h}{U_c} + \frac{h}{U_-} + \psi, \tag{3.5}$$

where U_c and U_- are respectively the convection velocities of the downstream- and upstream-propagating waves that constitute the feedback loop, f_s is the screech frequency, h is the distance between the nozzle exit plane and the downstream reflection point, ψ accounts for any additional delay associated with different components of the feedback loop, and N is an integer value that can be considered as the number of concurrent disturbances in the acoustic feedback loop at any moment (Edgington-Mitchell 2019). By combining the relation between the wavenumber and the phase velocity of a wave, (3.5) can be written further as

$$(k_h - k_-) \times h + 2\pi f_s \psi = \Delta k \times h + 2\pi f_s \psi = 2\pi N, \tag{3.6}$$

where Δk is the wavenumber difference between the downstream-propagating K–H wavepacket and the upstream-propagating guided jet mode. Here, the downstream-propagating K–H wavepacket is considered to be neutrally stable and k_h is calculated by using U_c listed in table 2 for different screech modes. The wavenumber of the upstream-propagating guided jet mode k_- is obtained from the vortex-sheet model (3.1), and ψ is assumed to be 0, i.e. the in-phase resonance criterion is considered. Using the dispersion relations of the downstream- and upstream-propagating waves, the frequencies at which (3.6) is satisfied are selected as the predicted frequencies.

For impinging jets, the impinging plate is usually viewed as the downstream reflection point, and h in (3.6) is equal to the impinging distance (Ho & Nosseir 1981; Bogey & Gojon 2017; Gojon & Bogey 2017). In the present study, not only the impinging distance at the jet axis ($5D$) but also the impinging distances along the upper and lower lip lines ($5.9D$ and $4.1D$) are used to predict tonal frequencies. As shown in figure 18, based on these three impinging distances, the frequencies and mode staging behaviours of acoustic resonances cannot be predicted. These results imply that the current acoustic resonances of underexpanded jets that impinge on an inclined plate are not due to the feedback loop between the nozzle exit and the plate.

The upstream- and downstream-propagating waves in the screech feedback loop are assumed to exchange energy at the nozzle exit and at a shock cell location, and the location of the fourth shock cell is used to predict screech frequencies in axisymmetric

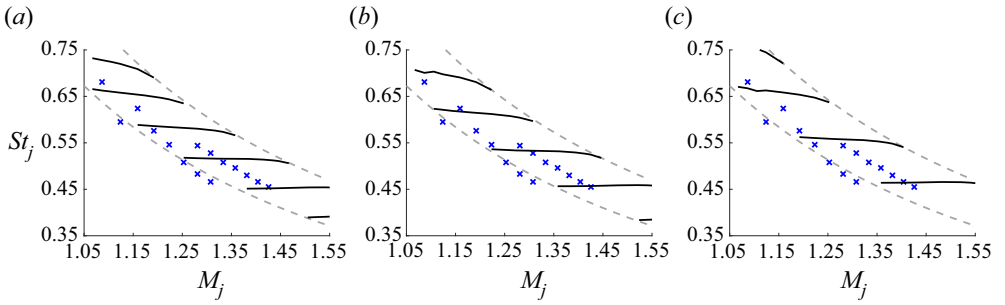

Figure 18. Comparison of acoustic resonance frequencies obtained from the acoustic measurements and the phase criterion (3.6) between the nozzle exit and the impinging plate: (*a*) $h = 5.9D$, the impinging distance at the upper lip line; (*b*) $h = 5.0D$, the impinging distance at the jet axis; and (*c*) $h = 4.1D$, the impinging distance at the lower lip line. The blue crosses indicate the results of acoustic measurements. The dashed grey lines indicate the frequency ranges in which the upstream-propagating guided jet mode (0, 2) is propagable.

A1 and A2 modes (Mancinelli *et al.* 2019, 2021). In this subsection, in order to predict tonal frequencies, the location of the downstream reflection point is determined by analysing the movements of upstream- and downstream-propagating waves relative to the averaged shock structures. The upstream- and downstream-propagating waves of the screech feedback loop are reconstructed approximately in § 3.6, and the movements of waves during half of the screech period are displayed in figure 19. In different screech modes, the parts with the same phases of the upstream- and downstream-propagating waves are encountered at the rear edge of the third shock cell. Therefore, the location of the third shock cell is considered as the downstream reflection point for different screech modes. It should be noted that as discussed in previous subsections, the acoustic resonance in different screech modes is associated with the interaction of the K–H wavepacket and shock cells in various axial regions. Thus identifying a specific location of interaction is inconstant and case-related. The location of this downstream reflection point is just used to predict resonance frequencies.

As shown in figure 4, the impinging plate has only slight effects on the first three shock cells. Thus h in (3.6) is calculated as $3 \times \lambda_s$, and the axial spacing of a shock cell λ_s is obtained by the formula of Pack (1950):

$$\frac{\lambda_s}{D} = \frac{\pi}{2.4048}\sqrt{M_j^2 - 1}. \tag{3.7}$$

Gojon *et al.* (2016) demonstrated that the number of cells in the standing wave pattern between the nozzle exit plane and the downstream reflection point is the N of (3.6). As shown in the normalized amplitude fields of figure 8, N is equal to 3, 4 and 5 for the A1, A2 and A3 modes, respectively. The reflection coefficients at the nozzle exit and the downstream reflection point are not accounted for in the present model. Thus this is a simplified version of the model in Mancinelli *et al.* (2021).

As shown in figure 20, based on the current experimental results, the screech frequencies calculated by (3.6) have good agreement with the results of acoustic measurements. By combining the phase criterion and the right parameters, screech frequencies of different screech modes can be predicted precisely (Nogueira *et al.* 2022*a*). As shown in figure 16, the vanishing of the A3 mode cannot be explained by combining the weakest link theory and the dispersion relation of the upstream-propagating guided jet mode. Thus the phase criterion for the A3 screech mode is examined further. At several M_j, the averaged schlieren

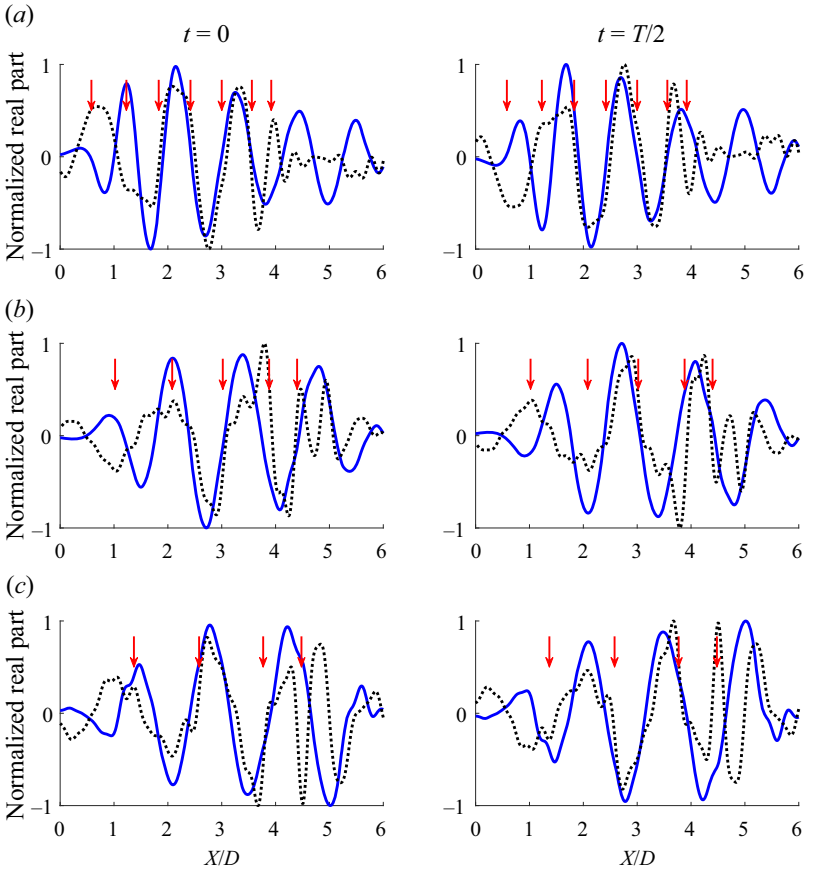

Figure 19. Movements of approximately reconstructed upstream- and downstream-propagating waves at the jet shear layer ($Y/D = 0.5$): (*a*) $M_j = 1.12$ jet (NPR = 2.20, A1 mode); (*b*) $M_j = 1.28$ jet (NPR = 2.70, A2 mode); and (*c*) $M_j = 1.40$ jet (NPR = 2.70, A2 mode). The approximately reconstructed upstream-propagating waves are indicated by the dashed black lines. The approximately reconstructed downstream-propagating waves are indicated by the solid blue lines. The red arrows indicate the axial positions of the shock reflection points at the jet shear layer.

images and the first SPOD modes at the screech frequencies of the A3 mode are shown in figure 21. There are always five cells in the standing wave pattern between the nozzle exit and the third shock reflection point along the upper lip line of jets. For the axisymmetric mode A3, the same phase criterion needs to be met at all the azimuthal positions. With the increase of M_j, the inclined plate gradually invades the third shock cell. In figures 21(*a–c*), the rear edge of the third shock cell is nearly vertical to the jet axis. The amplitudes of the standing wave patterns along the upper and lower lip lines are similar. As shown in figures 21(*d–f*), when M_j is larger than 1.40, the rear edge of the third shock cell is obviously inclined. The asymmetry of averaged shock structures and the differences between the h values along the upper and lower lip lines become distinct with the increase of M_j. The phase criterion is not satisfied at the lower side of the jet gradually. Thus the intensity of the standing wave pattern at the lower side becomes weaker relative to the upper side of the jets. When M_j is larger than 1.45, the jets would not generate the screech tone of the A3 mode.

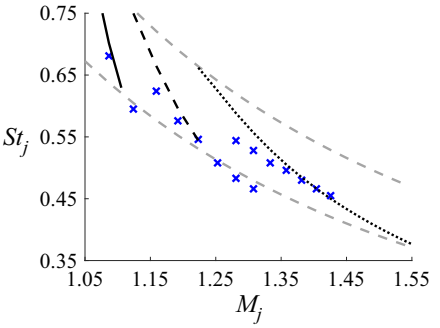

Figure 20. Comparison of acoustic resonance frequencies obtained from the acoustic measurements and the phase criterion (3.6) between the nozzle exit and the rear edge of the third shock cell. The blue crosses indicate the results of acoustic measurements. The dashed grey lines indicate the frequency ranges in which the upstream-propagating guided jet mode (0, 2) is propagable. The black solid, dashed and dotted lines indicate the results of the phase criteria of $N = 3$, 4 and 5, respectively.

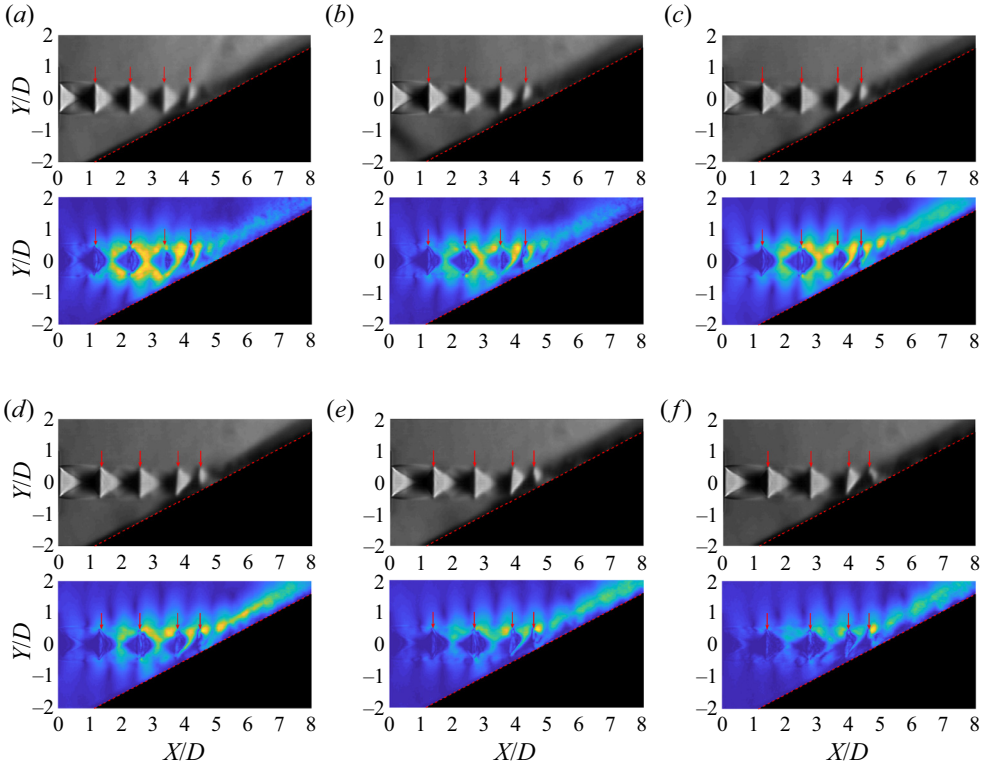

Figure 21. The first SPOD modes at the screech frequencies in A3 mode for the jets at (*a*) $M_j = 1.33$ ($St_j = 0.51$), (*b*) $M_j = 1.35$ ($St_j = 0.50$), (*c*) $M_j = 1.38$ ($St_j = 0.48$), (*d*) $M_j = 1.40$ ($St_j = 0.47$), (*e*) $M_j = 1.42$ ($St_j = 0.46$), and (*f*) $M_j = 1.44$ ($St_j = 0.45$). The top image of each panel is the averaged schlieren image. The bottom image of each panel is the normalized amplitude field of the SPOD mode. The colour scales range from 0 (blue) to 1 (yellow). The red arrows indicate the axial positions of the shock reflection points at the jet shear layer.

4. Conclusions

In the present study, acoustic measurements and high-speed schlieren visualizations are conducted to study the acoustic resonance mechanism for different axisymmetric screech modes of the underexpanded jets that impinge on an inclined plate. The nozzle-to-plate distance at the jet axis is set as $5.0D$, and the inclined angle of the plate is 30°. The ideally expanded jet Mach number ranges from 1.05 to 1.56. By comparing with the acoustic results of underexpanded free jets, the M_j range for the A2 screech mode of impinging jets is wider, and a new axisymmetric screech mode A3 appears in the acoustic spectra of impinging jets. The effect of the impinging plate on the shock cell structures of jets becomes obvious with the increase of M_j. The axial variations of shock cell spacings are more obvious near the impingement location. And the first and second suboptimal peaks are more distinct in the axial wavenumber spectra of averaged schlieren images.

The coherent flow structures that are associated with the acoustic resonances of different screech modes are extracted by SPOD, and the first SPOD modes at tonal frequencies are selected to be analysed. The chosen SPOD modes are further decomposed in the streamwise direction, and the axial wavenumber spectra suggest that the A1, A2 and A3 screech modes are respectively closed by the guided jet modes that are energized by the interactions between the Kelvin–Helmholtz wavepacket and the first three shock wavenumber peaks. The mode staging process for axisymmetric screech modes of impinging jets is analysed by combining the weakest link theory and the dispersion relations of upstream-propagating guided jet modes. The interaction between the K–H wavepacket and the first three peak wavenumbers of averaged shock structures leads to a redistribution of energy. At screech frequencies of the A1, A2 and A3 modes, the interaction wavenumbers of the first three shock wavenumber peaks are respectively located in the frequency ranges where the upstream-propagating guided jet modes are propagable. However, this methodology cannot explain the vanishing of the A3 screech mode.

The upstream- and downstream-propagating waves that constitute the screech feedback loop are reconstructed approximately based on the wavenumber spectra of the chosen SPOD modes. Taking the rear edge of the third shock cell as the downstream reflection point of the screech feedback loop, screech frequencies of different screech modes can be predicted by combining the phase criterion and the right parameters. For the A3 mode, with the increase of M_j, the inclined plate gradually invades the third shock cell, and the phase constraint cannot be satisfied at the lower side of jets for higher M_j, which leads to the vanishing of the screech tone in the A3 mode. The present results suggest that external boundaries can modulate the frequency and mode of jet screech by changing the axial wavenumbers of shock cells.

Funding. This work was supported by the National Key R&D Programme of China (grant no. 2022YFC2402600), the National Natural Science Foundation of China (grant nos 12202245, 11972215, 12072174), and the National Basic Research Programme of China (the 973 programme) through grant no. 2012CB720100. X.L. acknowledges financial support from the Shuimu Tsinghua Scholar Programme.

Declaration of interests. The authors report no conflict of interest.

Author ORCIDs.
Xiangru Li https://orcid.org/0000-0002-7817-2975;
Xuecheng Wu https://orcid.org/0000-0002-7091-0232;
Luhan Liu https://orcid.org/0000-0002-7926-9584;
Xiwen Zhang https://orcid.org/0000-0002-3706-4484;
Pengfei Hao https://orcid.org/0000-0002-7181-4322.

References

Akamine, M., Nakanishi, Y., Okamoto, K., Teramoto, S., Okunuki, T. & Tsutsumi, S. 2015 Acoustic phenomena from correctly expanded supersonic jet impinging on inclined plate. *AIAA J.* **53** (7), 2061–2067.

André, B., Castelain, T. & Bailly, C. 2014 Investigation of the mixing layer of underexpanded supersonic jets by particle image velocimetry. *Intl J. Heat Fluid Flow* **50**, 188–200.

Barone, M.F. & Lele, S.K. 2005 Receptivity of the compressible mixing layer. *J. Fluid Mech.* **540**, 301–335.

Berland, J., Bogey, C. & Bailly, C. 2007 Numerical study of screech generation in a planar supersonic jet. *Phys. Fluids* **19** (7), 075105.

Bogey, C. & Gojon, R. 2017 Feedback loop and upwind-propagating waves in ideally expanded supersonic impinging round jets. *J. Fluid Mech.* **823**, 562–591.

Brehm, C., Housman, J.A. & Kiris, C.C. 2016 Noise generation mechanisms for a supersonic jet impinging on an inclined plate. *J. Fluid Mech.* **797**, 802–850.

Davies, M.G. 1962 Tones from a choked axisymmetric jet II. The self excited loop and mode of oscillation. *Acustica* **12**, 267–277.

Edgington-Mitchell, D. 2019 Aeroacoustic resonance and self-excitation in screeching and impinging supersonic jets – a review. *Intl J. Aeroacoust.* **18** (2–3), 118–188.

Edgington-Mitchell, D., Jaunet, V., Jordan, P., Towne, A., Soria, J. & Honnery, D. 2018 Upstream-travelling acoustic jet modes as a closure mechanism for screech. *J. Fluid Mech.* **855**, R1.

Edgington-Mitchell, D., Li, X., Liu, N., He, F., Wong, T.Y., Mackenzie, J. & Nogueira, P. 2022 A unifying theory of jet screech. *J. Fluid Mech.* **945**, A8.

Edgington-Mitchell, D., Wang, T., Nogueira, P., Schmidt, O., Jaunet, V., Duke, D., Jordan, P. & Towne, A. 2021*a* Waves in screeching jets. *J. Fluid Mech.* **913**, A7.

Edgington-Mitchell, D., Weightman, J., Lock, S., Kirby, R., Nair, V., Soria, J. & Honnery, D. 2021*b* The generation of screech tones by shock leakage. *J. Fluid Mech.* **908**, A46.

Gojon, R. & Bogey, C. 2017 Flow structure oscillations and tone production in underexpanded impinging round jets. *AIAA J.* **55** (6), 1792–1805.

Gojon, R. & Bogey, C. 2019 Effects of the angle of impact on the aeroacoustic feedback mechanism in supersonic impinging planar jets. *Intl J. Aeroacoust.* **18** (2–3), 258–278.

Gojon, R., Bogey, C. & Marsden, O. 2016 Investigation of tone generation in ideally expanded supersonic planar impinging jets using large-eddy simulation. *J. Fluid Mech.* **808**, 90–115.

Gojon, R., Bogey, C. & Mihaescu, M. 2018 Oscillation modes in screeching jets. *AIAA J.* **56** (7), 2918–2924.

Henderson, B. 2002 The connection between sound production and jet structure of the supersonic impinging jet. *J. Acoust. Soc. Am.* **111** (2), 735–747.

Henderson, B., Bridges, J. & Wernet, M. 2005 An experimental study of the oscillatory flow structure of tone-producing supersonic impinging jets. *J. Fluid Mech.* **542**, 115–137.

Henderson, B. & Powell, A. 1993 Experiments concerning tones produced by an axisymmetric choked jet impinging on flat plates. *J. Sound Vib.* **168** (2), 307–326.

Ho, C.-M. & Nosseir, N.S. 1981 Dynamics of an impinging jet. Part 1. The feedback phenomenon. *J. Fluid Mech.* **105**, 119–142.

Jordan, P. & Colonius, T. 2013 Wave packets and turbulent jet noise. *Annu. Rev. Fluid Mech.* **45**, 173–195.

Karami, S., Stegeman, P.C., Ooi, A., Theofilis, V. & Soria, J. 2020 Receptivity characteristics of under-expanded supersonic impinging jets. *J. Fluid Mech.* **889**, A27.

Lamont, P.J. & Hunt, B.L. 1980 The impingement of underexpanded, axisymmetric jets on perpendicular and inclined flat plates. *J. Fluid Mech.* **100** (3), 471–511.

Lessen, M., Fox, J.A. & Zien, H.M. 1965 The instability of inviscid jets and wakes in compressible fluid. *J. Fluid Mech.* **21** (1), 129–143.

Li, X., Liu, N., Hao, P., Zhang, X. & He, F. 2021 Screech feedback loop and mode staging process of axisymmetric underexpanded jets. *Exp. Therm. Fluid Sci.* **122**, 110323.

Li, X.-R., Zhang, X.-W., Hao, P.-F. & He, F. 2020 Acoustic feedback loops for screech tones of underexpanded free round jets at different modes. *J. Fluid Mech.* **902**, A17.

Mancinelli, M., Jaunet, V., Jordan, P. & Towne, A. 2019 Screech-tone prediction using upstream-travelling jet modes. *Exp. Fluids* **60** (1), 1–9.

Mancinelli, M., Jaunet, V., Jordan, P. & Towne, A. 2021 A complex-valued resonance model for axisymmetric screech tones in supersonic jets. *J. Fluid Mech.* **928**, A32.

Manning, T. & Lele, S. 1998 Numerical simulations of shock–vortex interactions in supersonic jet screech. *AIAA Paper* 1998-282.

MERCIER, B., CASTELAIN, T. & BAILLY, C. 2017 Experimental characterisation of the screech feedback loop in underexpanded round jets. *J. Fluid Mech.* **824**, 202–229.
MITCHELL, D.M., HONNERY, D.R. & SORIA, J. 2012 The visualization of the acoustic feedback loop in impinging underexpanded supersonic jet flows using ultra-high frame rate schlieren. *J. Vis.* **15** (4), 333–341.
NOGUEIRA, P.A.S., JAUNET, V., MANCINELLI, M., JORDAN, P. & EDGINGTON-MITCHELL, D. 2022*a* Closure mechanism of the A1 and A2 modes in jet screech. *J. Fluid Mech.* **936**, A10.
NOGUEIRA, P.A.S., JORDAN, P., JAUNET, V., CAVALIERI, A.V.G., TOWNE, A. & EDGINGTON-MITCHELL, D. 2022*b* Absolute instability in shock-containing jets. *J. Fluid Mech.* **930**, A10.
NOGUEIRA, P.A.S., SELF, H.W.A., TOWNE, A. & EDGINGTON-MITCHELL, D. 2022*c* Wave-packet modulation in shock-containing jets. *Phys. Rev. Fluids* **7** (7), 074608.
NONOMURA, T., GOTO, Y. & FUJII, K. 2011 Aeroacoustic waves generated from a supersonic jet impinging on an inclined flat plate. *Intl J. Aeroacoust.* **10** (4), 401–425.
NONOMURA, T., HONDA, H., NAGATA, Y., YAMAMOTO, M., MORIZAWA, S., OBAYASHI, S. & FUJII, K. 2016 Plate-angle effects on acoustic waves from supersonic jets impinging on inclined plates. *AIAA J.* **54** (3), 816–827.
PACK, D.C. 1950 A note on Prandtl's formula for the wave-length of a supersonic gas jet. *Q. J. Mech. Appl. Maths* **3** (2), 173–181.
PANDA, J. 1999 An experimental investigation of screech noise generation. *J. Fluid Mech.* **378**, 71–96.
POWELL, A. 1953 On the mechanism of choked jet noise. *Proc. Phys. Soc.* **66** (12), 1039.
POWELL, A., UMEDA, Y. & ISHII, R. 1992 Observations of the oscillation modes of choked circular jets. *J. Acoust. Soc. Am.* **92** (5), 2823–2836.
RAMAN, G. 1999 Supersonic jet screech: half-century from Powell to the present. *J. Sound Vib.* **225** (3), 543–571.
SCHMID, P.J. 2010 Dynamic mode decomposition of numerical and experimental data. *J. Fluid Mech.* **656**, 5–28.
SCHMIDT, O.T. & COLONIUS, T. 2020 Guide to spectral proper orthogonal decomposition. *AIAA J.* **58** (3), 1023–1033.
SHARIFF, K. & MANNING, T.A. 2013 A ray tracing study of shock leakage in a model supersonic jet. *Phys. Fluids* **25** (7), 076103.
SHEN, H. & TAM, C.K.W. 2002 Three-dimensional numerical simulation of the jet screech phenomenon. *AIAA J.* **40** (1), 33–41.
SUZUKI, T. & LELE, S.K. 2003 Shock leakage through an unsteady vortex-laden mixing layer: application to jet screech. *J. Fluid Mech.* **490**, 139–167.
TAM, C.K.W. 1995 Supersonic jet noise. *Annu. Rev. Fluid Mech.* **27** (1), 17–43.
TAM, C.K.W. 2009 Mach wave radiation from high-speed jets. *AIAA J.* **47** (10), 2440–2448.
TAM, C.K.W. & AHUJA, K.K. 1990 Theoretical model of discrete tone generation by impinging jets. *J. Fluid Mech.* **214**, 67–87.
TAM, C.K.W. & HU, F.Q. 1989 On the three families of instability waves of high-speed jets. *J. Fluid Mech.* **201**, 447–483.
TAM, C.K.W., PARRISH, S.A. & VISWANATHAN, K. 2014 Harmonics of jet screech tones. *AIAA J.* **52** (11), 2471–2479.
TAM, C.K.W., SEINER, J.M. & YU, J.C. 1986 Proposed relationship between broadband shock associated noise and screech tones. *J. Sound Vib.* **110** (2), 309–321.
TAM, C.K.W. & TANNA, H.K. 1982 Shock associated noise of supersonic jets from convergent–divergent nozzles. *J. Sound Vib.* **81** (3), 337–358.
TOWNE, A., CAVALIERI, A.V.G., JORDAN, P., COLONIUS, T., SCHMIDT, O., JAUNET, V. & BRÈS, G.A. 2017 Acoustic resonance in the potential core of subsonic jets. *J. Fluid Mech.* **825**, 1113–1152.
TOWNE, A., SCHMIDT, O.T. & COLONIUS, T. 2018 Spectral proper orthogonal decomposition and its relationship to dynamic mode decomposition and resolvent analysis. *J. Fluid Mech.* **847**, 821–867.
WEIGHTMAN, J.L., AMILI, O., HONNERY, D., EDGINGTON-MITCHELL, D. & SORIA, J. 2019 Nozzle external geometry as a boundary condition for the azimuthal mode selection in an impinging underexpanded jet. *J. Fluid Mech.* **862**, 421–448.
WEIGHTMAN, J.L., AMILI, O., HONNERY, D., EDGINGTON-MITCHELL, D.M. & SORIA, J. 2017*a* On the effects of nozzle lip thickness on the azimuthal mode selection of a supersonic impinging flow. *AIAA Paper* 2017-3031.
WEIGHTMAN, J.L., AMILI, O., HONNERY, D., SORIA, J. & EDGINGTON-MITCHELL, D. 2017*b* An explanation for the phase lag in supersonic jet impingement. *J. Fluid Mech.* **815**, R1.